

TI - The role of nano-perovskite in the negligible thorium release in seawater from Greek bauxite residue (red mud)

JA - Scientific Reports

PY - **2016**/02/22/online

VL - **6**

SP - **21737**

UR - <http://dx.doi.org/10.1038/srep21737>

# SCIENTIFIC REPORTS

OPEN

## The role of nano-perovskite in the negligible thorium release in seawater from Greek bauxite residue (red mud)

Received: 06 August 2015

Accepted: 25 January 2016

Published: 22 February 2016

Platon N. Gamaletsos<sup>1,2,6</sup>, Athanasios Godelitsas<sup>2</sup>, Takeshi Kasama<sup>1</sup>, Alexei Kuzmin<sup>3</sup>, Markus Lagos<sup>4</sup>, Theo J. Mertzimekis<sup>5</sup>, Jörg Göttlicher<sup>6</sup>, Ralph Steininger<sup>6</sup>, Stelios Xanthos<sup>7,8</sup>, Yiannis Pontikes<sup>9</sup>, George N. Angelopoulos<sup>10</sup>, Charalampos Zarkadas<sup>11</sup>, Aleksandr Komelkov<sup>11</sup>, Evangelos Tzamos<sup>12</sup> & Anestis Filippidis<sup>12</sup>

We present new data about the chemical and structural characteristics of bauxite residue (BR) from Greek Al industry, using a combination of microscopic, analytical, and spectroscopic techniques. SEM-EDS indicated a homogeneous dominant "Al-Fe-Ca-Ti-Si-Na-Cr matrix", appearing at the microscale. The bulk chemical analyses showed considerable levels of Th ( $111 \mu\text{g g}^{-1}$ ), along with minor U ( $15 \mu\text{g g}^{-1}$ ), which are responsible for radioactivity ( $355$  and  $133 \text{ Bq kg}^{-1}$  for  $^{232}\text{Th}$  and  $^{238}\text{U}$ , respectively) with a total dose rate of  $295 \text{ nGy h}^{-1}$ . Leaching experiments, in conjunction with SF-ICP-MS, using Mediterranean seawater from Greece, indicated significant release of V, depending on S/L ratio, and negligible release of Th at least after 12 months leaching. STEM-EDS/EELS & HR-STEM-HAADF study of the leached BR at the nanoscale revealed that the significant immobility of  $\text{Th}^{4+}$  is due to its incorporation into an insoluble perovskite-type phase with major composition of  $\text{Ca}_{0.8}\text{Na}_{0.2}\text{TiO}_3$  and crystallites observed in nanoscale. The Th  $L_{III}$ -edge EXAFS spectra demonstrated that  $\text{Th}^{4+}$  ions, which are hosted in this novel nano-perovskite of BR, occupy  $\text{Ca}^{2+}$  sites, rather than  $\text{Ti}^{4+}$  sites. That is most likely the reason of no Th release in Mediterranean seawater.

Worldwide, the refining of bauxite ore deposits to alumina through the Bayer process results in production of huge quantities of a solid metallurgical bauxite residue (BR), the so-called "red mud". It is estimated that 2 metric tones of BR are produced per ton of alumina ( $\text{Al}_2\text{O}_3$ ) and, moreover, that up to  $120 \times 10^6$  metric tones of this residual material are deposited every year by the global Al industry e.g.<sup>1,2</sup>. The sustainable storage of BR in enormous quantities raises severe concerns on the design, construction and operation of their reservoir, directly related to economic, spatial, technological and environmental issues e.g.<sup>3,4</sup>. For instance, the major deadly accident happened in Hungary around the Ajkai Timföldgyár alumina plant on 4<sup>th</sup> October 2010 e.g.<sup>5,6</sup>. In that accident, it was proved that BR acted as a significant source of V, and As in the environment<sup>1,7</sup> whereas radioactivity issues, due to  $^{232}\text{Th}$ ,  $^{238}\text{U}$ , and  $^{40}\text{K}$ , have also raised concern<sup>8</sup>.

<sup>1</sup>Center for Electron Nanoscopy, Technical University of Denmark, 2800 Kongens Lyngby, Denmark. <sup>2</sup>Faculty of Geology & Geoenvironment, National and Kapodistrian University of Athens, Zografou Campus, 15784 Athens, Greece. <sup>3</sup>Institute of Solid State Physics, University of Latvia, Kengaraga str. 8, 1063 Riga, Latvia. <sup>4</sup>Karlsruhe Institute of Technology, Institute for Nuclear Waste Disposal, Hermann-von-Helmholtz-Platz 1, 76344 Eggenstein-Leopoldshafen, Germany. <sup>5</sup>Faculty of Physics, National and Kapodistrian University of Athens, Zografou Campus, 15784 Athens, Greece. <sup>6</sup>Karlsruhe Institute of Technology, ANKA Synchrotron Radiation Facility, Hermann-von-Helmholtz-Platz 1, 76344 Eggenstein-Leopoldshafen, Germany. <sup>7</sup>Department of Electrical and Computer Engineering, Nuclear Technology Laboratory, Aristotle University of Thessaloniki, 54124 Thessaloniki, Greece. <sup>8</sup>Department of Automation Engineering, Alexander Technological Educational Institute of Thessaloniki, 57400 Thessaloniki, Greece. <sup>9</sup>KU Leuven, Department of Materials Engineering, Kasteelpark Arenberg 44, 3001 Leuven, Belgium. <sup>10</sup>University of Patras, Department of Chemical Engineering, 26500 Rio, Greece. <sup>11</sup>PANalytical B.V., 7600 AA Almelo, The Netherlands. <sup>12</sup>School of Geology, Aristotle University of Thessaloniki, 54124, Thessaloniki, Greece. Correspondence and requests for materials should be addressed to P.N.G. (email: plagka@dtu.dk)

Nowadays, according to U.S. Geological Survey (USGS), Greece is considered the 16<sup>th</sup> alumina (Al<sub>2</sub>O<sub>3</sub>) producer in the world and the 4<sup>th</sup> among the E.U. member-states. In Greece, the production of BR from the “Aluminium of Greece S.A.” at its processing plant in Agios Nikolaos area (Antikyra bay, Gulf of Corinth) is approx.  $500\text{--}680 \times 10^3$  metric tonnes per year<sup>9,10</sup>. As per previous regulations, the plant was allowed to pump the BR directly to the bottom of the sea, at the depth of > 100 m. Since 2007, this practice has gradually ceased and through substantial investments (i.e., four filter presses to deliver a semi-dry cake, a new disposal area, a number of research projects for valorization trajectories and more) BR is currently industrially utilized in cement production, with ongoing efforts in the area of ceramics and metallurgy e.g.<sup>11–13</sup>. Due to the former disposal practice, millions of metric tonnes of BR are still remaining on the sea bed of the Antikyra bay e.g.<sup>14,15</sup>, fostering the debate on the potential impact of BR to the marine environment. At the same time, the BR potentially acts as alternative resource of strategic metals and that is of great concern, too. Previous studies have been carried out to elucidate the basic chemical composition and distribution of the discharged BR onto the bottom of sea e.g.<sup>14,15</sup> and to address the issue of the nature of actinides in BR<sup>11,12</sup>. Claims on elevated radioactivity, mainly due to <sup>232</sup>Th-series, and potential release of radionuclides in the environment of the Antikyra Bay were also indicated<sup>16–18</sup>. It is noteworthy to mention that an industrial scale pilot plant (the so-called “ENEXAL” BR treatment process e.g.<sup>19,20</sup>), resulting in the full conversion of BR into pig iron and mineral wool, has been recently applied mainly by the “Aluminium of Greece S.A.”. On the other hand, the determination of rare earth elements/REEs (i.e., lanthanides + Y + Sc) in BR, and the subsequent recovery of REEs using acids has also been reported<sup>3,4,21–26</sup>.

The fact that Th, which is primarily present in the minerals of the initial bauxite ore e.g.<sup>27,28</sup>, is subsequently transferred into BR through the Bayer process<sup>11,12</sup>, puts forward the claim that the deep knowledge about the localization of this actinide is mandatory, due to its environmental concern in the mining and metallurgical industry. However, the exact nature of this actinide element in the above natural (parent bauxite) and synthetic (bauxite metallurgical residue/BR) materials has been rather unknown, until the present paper. Hence, the scope of this study was to provide a thorough study on Greek BR with new insights, giving emphasis to the solid-state characterization of metals and metalloids, particularly to the nature of Th -related to radioactivity- and, in addition, to the mobility of these elements into the Mediterranean seawater. To the best of our knowledge, this is the first time in the literature that the leachability of BR in seawater is demonstrated. Leaching tests with acetic acid, instead of typical toxicity characteristic leaching procedure (TCLP) or by other conventional sequential extraction procedure<sup>29</sup> modified after Tessier *et al.* (1979)<sup>30</sup>, as recently proposed in the case of potentially hazardous elements in BR<sup>31</sup>, were specifically applied for Th, REEs, and selected high field strength elements/HFSE (Nb, Ta), in long intervals (2 weeks to 1 year). Similar leaching experiments were additionally performed using Greek bauxites for comparative reasons. It should be mentioned that the thorough investigation of actinides, and namely of Th, aiming at the chemical behavior of the contaminant in the environment, has never been carried out with regard to BR originating from Greece; previous studies in Japan<sup>32</sup> and recently in China<sup>29,33</sup> have reported the problem. It is notable that although Gu & Wang (2013)<sup>29</sup> have studied Th-rich ( $88\text{--}257 \mu\text{g g}^{-1}$ ) red mud by conventional transmission electron microscopy (TEM) the “accessory” and/or “neo-formational minerals” hosting the actinide element have never been determined. Of note, the structural environment of Th, particularly by extended X-ray absorption fine structure spectroscopy (EXAFS), has not been documented in the literature so far as in the case of other metals sorbed by Australian BR<sup>34</sup>. The final perspective of the present paper is to prospectively try to contribute to one of the world’s largest chronic problems, concerning the reuse of mining and mineral-processing residues and industrial wastes e.g.<sup>35</sup> affecting the future of sustainable development<sup>36</sup>. The criticality of global aluminum demand<sup>37,38</sup>, resulting in the expansion of the Al industry and relevant solid wastes, enhances the necessity for detailed studies on the chemical, structural and environmental characteristics of BR. In conclusion, we consider that the study of actinides, and namely Th, in alumina refineries’ products can redound to a sustainable supply of strategic metals and oxides, and thus contribute to a more sustainable “modus operandi”.

## Results & Discussion

**Bulk and microscale characterization.** Concerning the raw BR sample Fe, Al, Ca, Ti, Na, Si, O and H, are the elements corresponding to solids detected by powder X-ray diffraction/PXRD (see Supplementary Information and Supplementary Fig. S1), while phases related to other elements of interest, such as actinides (namely Th), Cr, V, As, Pb, as well as REEs, are not detectable. The same applies for the seawater- and the acid-treated BR samples. However, Cr, along with the above major elements, is additionally indicated by scanning electron microscopy (SEM) equipped with an energy dispersive spectrometry (EDS), into an “Al-Fe-Ca-Ti-Si-Na-Cr matrix” appearing in a few  $\mu\text{m}$  size (Fig. 1). Since all the micro areas of the raw sample, checked by SEM-EDS, follow the same spectral pattern and, therefore, it is argued that the raw BR is apparently rather homogeneous in terms of composition at the microscale. Taking into account the PXRD patterns, it could be assumed that this matrix is an admixture of nanocrystalline phases and potential amorphous and/or poorly crystalline phases.

The wavelength dispersive X-ray fluorescence (WDXRF) and, complementary, the inductively coupled plasma mass and optical emission spectroscopic measurements (ICP-MS/OES) of the studied BR proved that major Fe, Al, Ca, Si, Ti, Na and C, as well as significant volatiles (loss on ignition/LOI) comprise 86.5 wt.% and 13.6 wt.% of its chemical composition, respectively. In addition, when the trace elements’ concentrations of BR are normalized to the average values of Greek bauxites ( $n = 16$ )<sup>28</sup> and of Upper Continental Crust (UCC) e.g.<sup>28</sup> and references therein, depletion in Ga (following the chemical behavior of Al) and enrichment -among others- in Cr ( $2403 \mu\text{g g}^{-1}$ ), V ( $1081 \mu\text{g g}^{-1}$ ), Ni ( $902 \mu\text{g g}^{-1}$ ), As ( $164 \mu\text{g g}^{-1}$ ), Pb ( $120 \mu\text{g g}^{-1}$ ), Sc ( $114 \mu\text{g g}^{-1}$ ) as well as in Cd, but also in Nb, Y, Ta, and REEs (Supplementary Table S3 and Supplementary Fig. S2) is pointed out. Moreover, high levels of Th ( $111 \mu\text{g g}^{-1}$ ) have been determined using high-resolution (HR)  $\gamma$ -ray spectroscopy; rather higher than those reported in the literature<sup>28,39</sup> and references therein. The latter, and also minor U content ( $15 \mu\text{g g}^{-1}$ ), are responsible for the radioactivity of the studied BR ( $355 \text{ Bq kg}^{-1}$  for <sup>232</sup>Th and  $133 \text{ Bq kg}^{-1}$  for <sup>238</sup>U) with a total dose rate of  $295 \text{ nGy h}^{-1}$  (see Supplementary Table S4). It should be mentioned that the radioactivity of Greek BR due to Th is in the

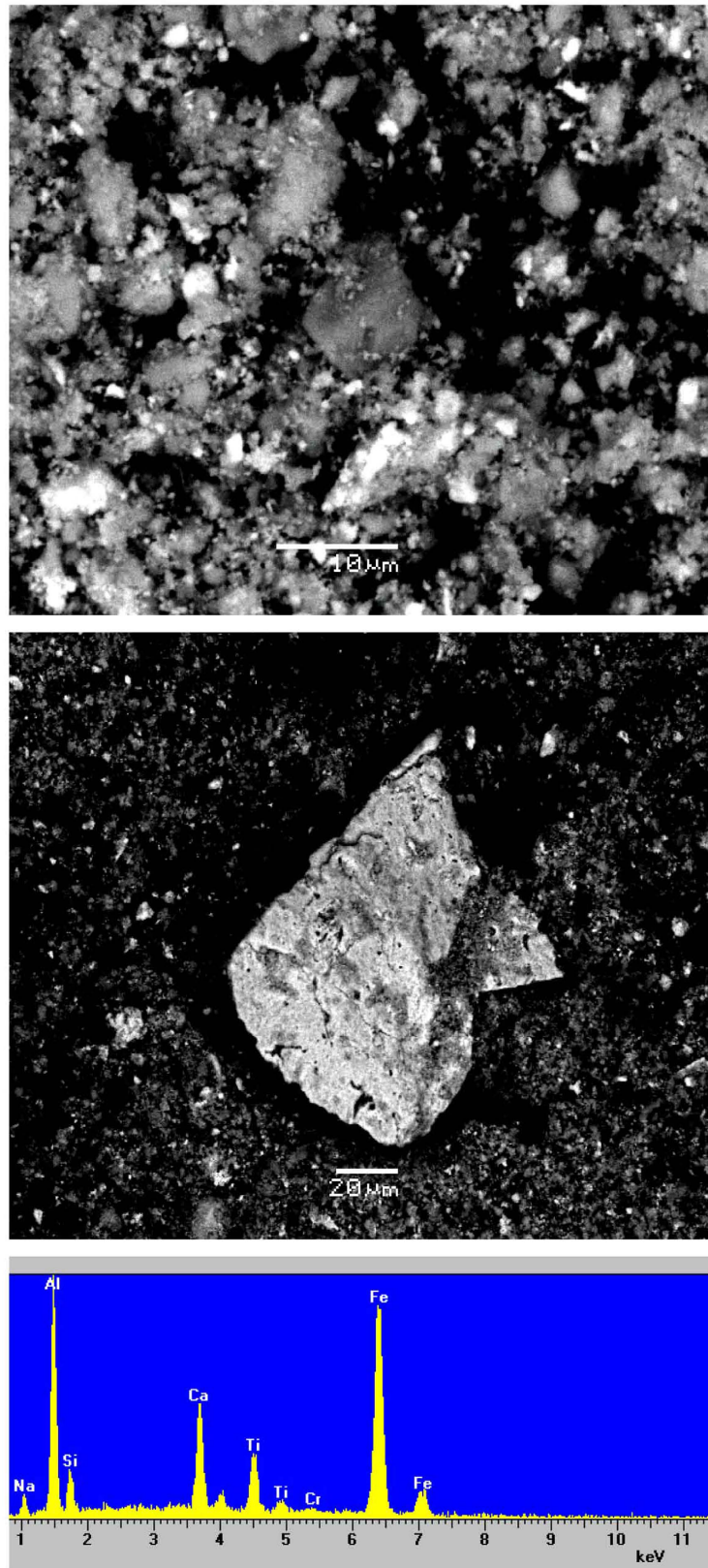


**Figure 1.** Morphology and chemical composition (major elements) of bauxite residue/BR (red mud) at the microscale, obtained by SEM-EDS, indicating the “Al-Fe-Ca-Ti-Si-Na-Cr matrix” which was further subjected to nanoscale study (see Figs 3 and 4).

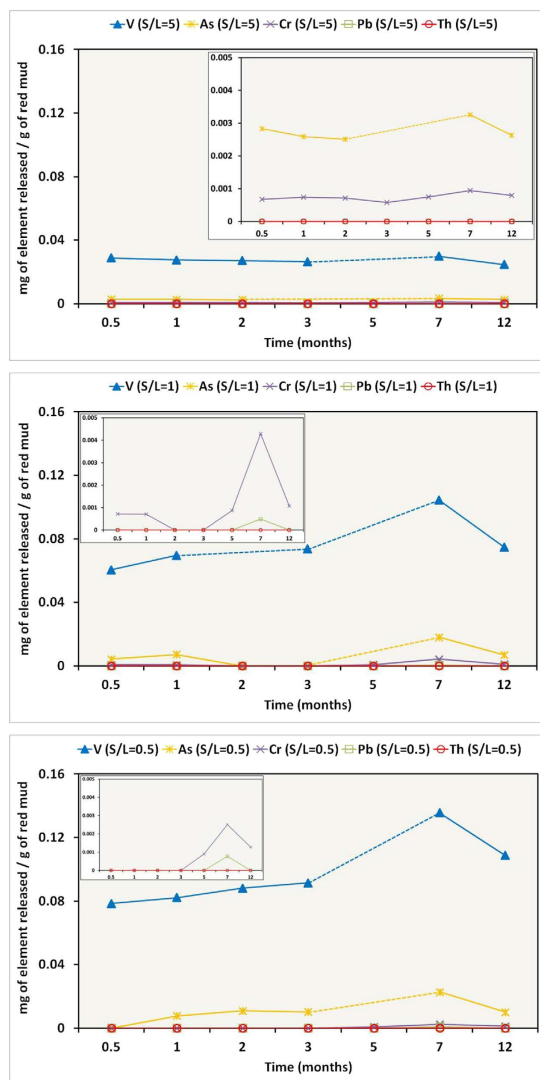


**Figure 2.** Results from leaching experiments of bauxite residue/BR (red mud) with Mediterranean seawater and variable S/L ratios, concerning V, As, Cr, Pb and Th.

same range from other BR reservoirs around the world, with the exception of the Australian BR, reaching up to  $1900 \text{ Bq kg}^{-1}$  (see Supplementary Table S4 and references therein). The studied BR has higher Th radioactivity compared to the average of the studied Greek bauxites from Parnassos-Ghiona mines (avg.  $182 \text{ Bq kg}^{-1}$ ; avg. total dose rate:  $162 \text{ nGy h}^{-1}$ ;  $n = 10$ ). The same stands for radioactivity due to U, whereas both materials exhibit similar values due to  $^{40}\text{K}$ .

**Leaching experiments.** Leaching experiments for the studied BR, in conjunction with sector field (SF) ICP-MS spectroscopy using Mediterranean seawater from Greece indicated significant release of V, relatively to seawater composition<sup>40</sup>, depending on S/L ratio (Fig. 2). Thus, V appears to be the most mobile element, perhaps due to its major association with rather soluble phases. This is in accordance with previous leaching NEN7341 tests concerning BR calcined in inert and reducing atmosphere<sup>11</sup>, as well as in good agreement with recent studies about V in Hungarian BR<sup>1,7</sup>. According to the latter studies, presenting X-ray absorption near-edge structure (XANES) spectroscopic data of vanadium (V K-edge), V in Hungarian BR is pentavalent associated with a Ca-Al-hydroxysilicate phase, corresponding to “hydrogarnet”-type phase. We can, therefore, assume that in Greek BR, having the same phase composition as the Hungarian BR, V is present most likely as  $\text{VO}_4^{3-}$  anions, known to be mobile in seawater. On the other hand, V in Australian BR has been reported as tetravalent and/or trivalent related to ilmenite and/or goethite<sup>41</sup>. However, ilmenite has not been detected in Greek BR so far using PXRD, SEM or TEM (see text below), whereas the actual presence of goethite, either at the microscale or at the nanoscale, cannot be confirmed with certainty. Traces of As and Cr have also been detected, relatively to seawater composition<sup>40</sup>, after prolonged exposure in lower solid-to-liquid (S/L) ratio, while Pb is practically immobile. Based on previous Cr K-edge XANES and TEM studies<sup>7,41</sup> Cr is associated with hematite showing less solubility. The most interesting point is that Th -related to radioactivity- seems to be immobile in seawater, at least after 12 months of leaching tests (Fig. 2). However, taking into account the PXRD study and the SEM-EDS investigation

of the BR (see text above), it can be stated that there is no clear evidence of the Th-hosting phase(s) in the Greek BR at the microscale. That was finally realized combining the data yielded by both the scanning transmission electron microscopy-energy dispersive spectroscopy (STEM-EDS) and the electron energy-loss spectroscopy (EELS) together with the Th  $L_{III}$ -edge EXAFS spectroscopic measurements on the studied BR (see text below). Analogous leaching experiments with the basic parent material (typical low-grade and high-grade Greek industrial bauxite) in Mediterranean seawater from Greece were carried out for comparative reasons; they showed negligible V, As, Cr, Pb, and Th release (Supplementary Fig. S3). The effect of S/L ratio is also depicted, indicating that lower S/L ratio causes a relative increase on the solubilization of heavy metals in the studied bauxites, during the experiments. Additional acetic acid-leaching experiments with the BR indicated significant release of V, as in the case of seawater, and much higher release of Cr (Supplementary Figs S4 and S5), a phenomenon also mentioned in the literature<sup>31</sup>. Nevertheless, it is worthy to note that the high release of REEs from BR (Supplementary Fig. S5), giving facts for potential recovery technologies inasmuch future availability of REEs is of great concern due to monopolistic supply conditions, environmentally unsustainable mining practices, and rapid demand growth<sup>42</sup>. This is in line with previous relevant works for Greek BR with regard to acid-recovery of lanthanides and Y<sup>21–24</sup>. In either case, the negligible effect of S/L ratio is also presented, indicating that the percentage of released elements -including the REEs- from leached BR is not severely affected by the S/L, during the experiment. Similar leaching experiments with typical low-grade (Fe-rich) and high-grade (Fe-depleted) Parnassos-Ghiona bauxites, presented for the first time in the literature, have also indicated significant recovery of REEs (Supplementary Figs S6 and S7). In the case of bauxites, the mobility of REE in acid is due to the presence of light REE (LREE) minerals (mostly bastnäsite/parisite-group) as reported previously<sup>27,28</sup>. Despite the fact that the mobility of Th in acid-treated bauxite residue is relatively enhanced, as compared to its negligible mobilization in seawater environment, considerable amount of this actinide element seems to remain in Greek BR. This robustly proves that the aforementioned acid-insoluble as well as seawater-insoluble solid nanophase (not apparent in the SEM-EDS observations) is hosting immobile Th into the “Al-Fe-Ca-Ti-Si-Na-Cr matrix”. The difference at the microscale between the initial (raw) and acid-treated “Al-Fe-Ca-Ti-Si-Na-Cr matrix” does affect mainly the lowering of Ca-K $\alpha$  X-ray emission peak in the EDS spectra (Fig. 1 and Supplementary Fig. S8) attributed to the loss of Ca-carbonate minerals and Ca-Al-hydroxysilicate phases.

**Nanoscale characterization.** Except for the aforementioned observed solid phases at the microscale (see text above) calcium titanium oxide (CTO) phases are expected to be produced due to the addition of lime during the Bayer process<sup>43</sup>, under low-T and low-P conditions. Regarding CTO in Greek BR, a calcium titanium oxide phase previously identified by bulk PXRD<sup>32</sup>, was arbitrarily reported as “perovskite”<sup>20,43</sup>. However, perovskite was detected by PXRD in BR from Zhengzhou Changcheng alumina plant in China<sup>43,44</sup>, from the Aughinish alumina plant in Ireland<sup>43,45,46</sup>, and from India<sup>43,47</sup>. On the other hand, Santini (2015)<sup>48</sup> in a similar study with regard to BR from USA, determined only sodalite- and cancrinite-phases but not any crystalline CTO and/or perovskite. Furthermore, conventional TEM “photographs” showed perovskite in BR from China<sup>49</sup> without any structural proof.

According to the STEM-EDS/EELS study (Figs 3 and 4 and Supplementary Figs S9–S12), the most motivating of the Ti-phases constituting the microscale “Al-Fe-Ca-Ti-Si-Na-Cr matrix” of the Greek BR is an unusual low-T and low-P perovskite-type phase e.g.<sup>50</sup> occurring in nanoscale (Fig. 3a,b). The major composition of this nano-perovskite has been determined by TEM-EDS to be  $\text{Ca}_{0.8}\text{Na}_{0.2}\text{TiO}_3$ . Since several other minor elements (such as Ce, Nb, Zr, Cr and, possibly, Sr) might additionally be hosted as impurities (Fig. 3c) that might lead us to argue about a Ca-Na-(Ce-Nb-Zr-Cr)-nano-perovskite. This argument implies a minor contribution of Ce-loparite-type phase ( $\text{Ce}(\text{Ti},\text{Nb})\text{O}_3$ ). The most important finding is that this nano-perovskite contains Th (Fig. 3c), which is estimated to be  $700\ \mu\text{g g}^{-1}$ . The STEM imaging, generated by the high angle annular dark field (HAADF) detector, together with the STEM-EDS mapping (Fig. 3d), clearly showed the distribution of key elements (such as Na, Ca, Ti, and O) for the Th-hosting nano-perovskite (CTO) that co-exists with other neighboring mineral phases (hematite and clay-like phases; see text below) into the “Al-Fe-Ca-Ti-Si-Na-Cr matrix”. In the depicted EDS maps Fe is exclusively attributed to the neighboring hematite, while Al is due to the clay-like phase. All the obtained selected area electron diffraction (SAED) patterns from nano-perovskite correspond to a perovskite structure [lattice parameters are a:  $0.562 (\pm 0.02)$  nm, b:  $0.752 (\pm 0.02)$  nm and c:  $0.561 (\pm 0.02)$  nm,  $Pnma$ ) with superlattice reflections (Fig. 3a)]. Since these reflections do not exist in the conventional perovskite we assume that they might be associated with the substitution of Na on A-site. It has recently reported that Na may incorporate into A-site of a  $\text{ABO}_3$  and BST perovskite, when synthesized at high-T or at high-P<sup>51–53</sup>, but that has never been observed at low-T and low-P perovskites. According to recent discussion by Seki *et al.* (2014)<sup>53</sup>, Na-ions could be linked with tilting of  $\text{TiO}_6$  octahedra, causing significantly stronger superlattice reflections in Ca-containing perovskites. Additional structural information on the novel  $\text{Ca}_{0.8}\text{Na}_{0.2}\text{TiO}_3$  is obtained by EELS measurements (see Supplementary Information and Supplementary Fig. S9). As it has already been mentioned, the BR nano-perovskite occurs together with Th-free Ti-containing hematite particles (Fig. 4). The concentration of Ti in this Ti-containing hematite has been measured up to 5 wt.%. Small amounts of Si, Al, Cr (Fig. 4b) and, probably, P (Supplementary Fig. S10) also exist in the Ti-containing hematite. Distinct Th-free Ti-oxides were characterized as anatase (Fig. 4c and Supplementary Fig. S11). The anatase crystallites exhibit rounded shape with a smooth surface. When the STEM-EDS spectra of Th-free Ti-containing hematite and anatase are compared with the EDS spectrum of the Th-containing nano-perovskite the total absence of Th is obvious (Fig. 4d). Concurrently, EDS artifacts like escape peaks for Ti K $\alpha$  and Ti K $\beta$  are also present. The peak ratio of Th M $\alpha$  and Th M $\beta$  was found to be about 5:3, which is in good agreement with the experimental profile, although the second broad peak (3.15 KeV) may be partially affected by the Ti K $\beta$  escape peak at 3.18 KeV (Fig. 4d). Besides, several planar defects, common found in anatase, have been demonstrated by high-resolution TEM (HRTEM) imaging (a,b of Supplementary Fig. S11). Subsequently, the STEM-HAADF and HR-STEM-HAADF observations

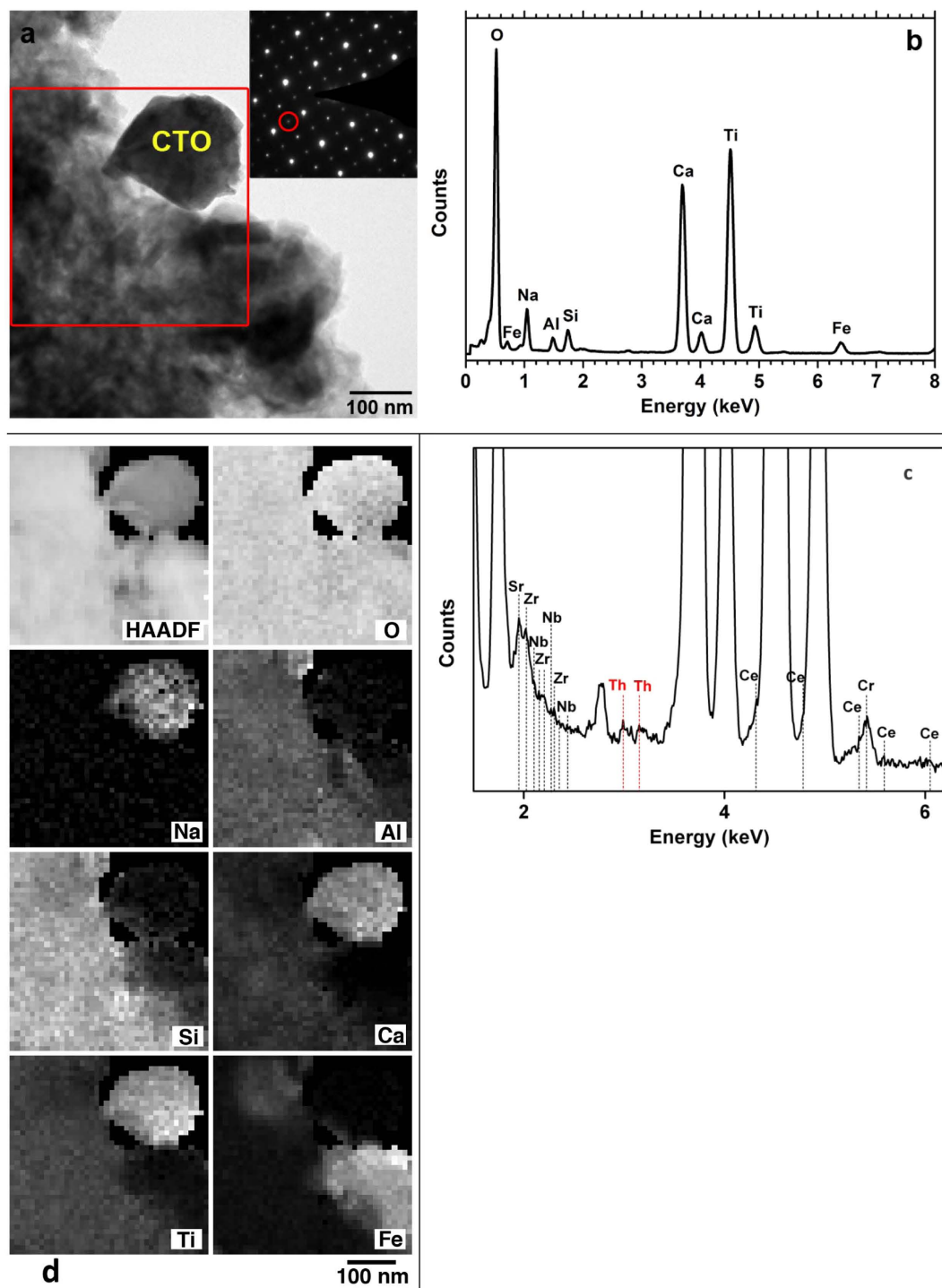


**Figure 3.** STEM-EDS data concerning a representative Th-hosting nano-perovskite ( $\text{Ca}_{0.8}\text{Na}_{0.2}\text{TiO}_3/\text{CTO}$ ) into bauxite residue (BR). Bright Field (BF) image and SAED pattern (a); STEM-EDS spectrum (b); enlarged energy area of the spectrum showing the presence of Th and minor elements (c). The viewing direction for the acquisition of SAED pattern is [101]. A peak at 452 eV is due to Ti  $L\alpha$ , while a second peak at 2.77 KeV and a third peak at 1.95 keV are attributed to the Si escape peak for Ti  $K\alpha$  and for Ca  $K\alpha$ , respectively; the latter one overlaps with the Sr, Nb and Zr peaks (c). The red-colored rectangle in the BF image indicates the area where the STEM-HAADF image and the EDS elemental maps were recorded. Superlattice reflections at the SAED pattern are marked with red-colored circle. STEM-HAADF image and EDS elemental maps (grayscale range of O: 0–62%; Na: 0–6%; Al: 0–17%; Si: 0–21%; Ca: 0–16%; Ti: 0–24%; Fe: 0–51%) for nano-perovskite crystallite (d). Fe is attributed to the neighboring Ti-containing hematite and the clay-like phases (see also Supplementary Fig. S11).

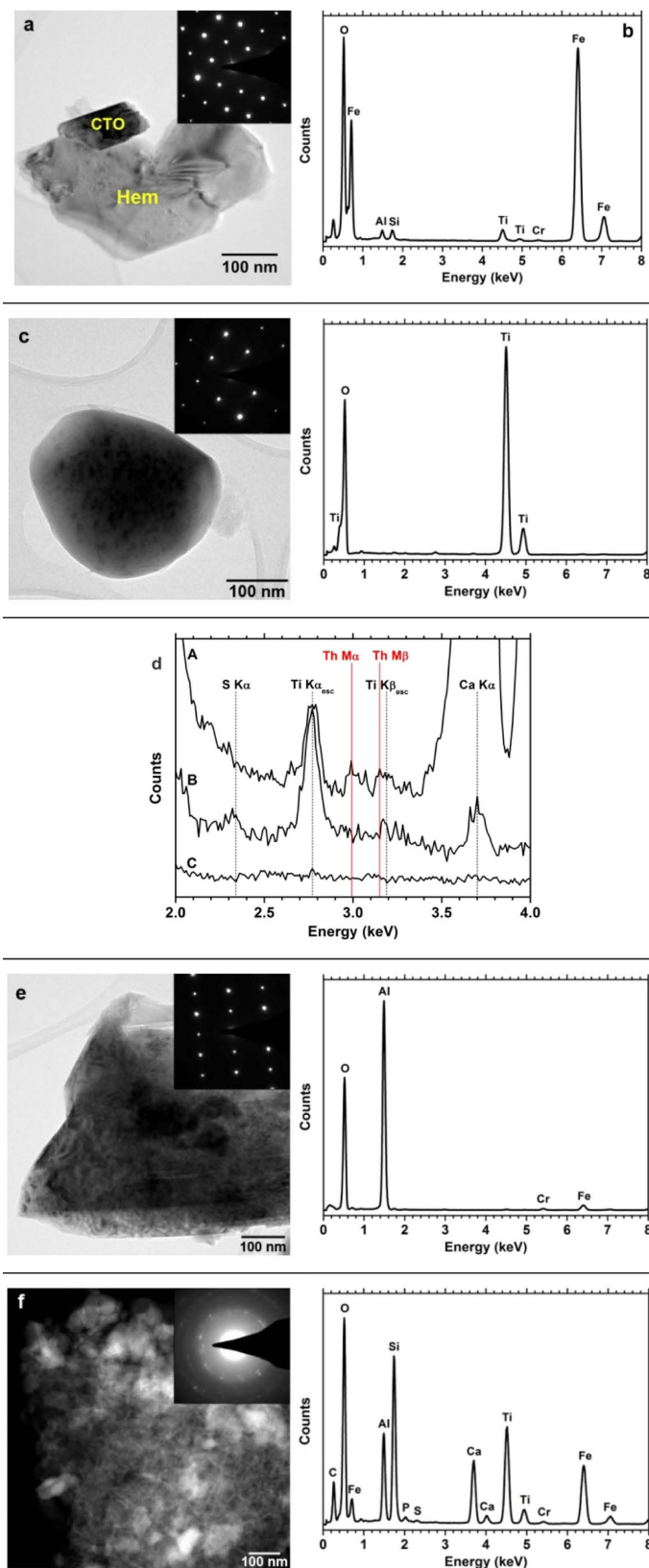


**Figure 4.** STEM-EDS data for Ti-containing hematite (Hem) particles intergrown with nano-perovskite (CTO). BF image and SAED pattern (acquired from [211] viewing direction; **a**) and the corresponding STEM-EDS spectrum (**b**, see also Supplementary Fig. S9). The almost visible narrow peak of Na is due to background noise. STEM-EDS data for anatase particle, including a BF image and SAED pattern as well as a STEM-EDS spectrum (**c**). The viewing direction for SAED pattern is [111]. A peak at 2.77 KeV is related to the Si escape peak for Ti K $\alpha$ , while a peak at 3.19 KeV can be assigned as the Si escape peak for Ti K $\beta$ . Comparison (**d**) between the

STEM-EDS spectra of Th-hosting nano-perovskite (a), Th-free anatase (b) and Th-free Ti-containing hematite (c). The Th  $M\alpha$  and Th  $M\beta$  peaks are demonstrated (red lines) together with the STEM-EDS artefacts of the escape peaks for Ti  $K\alpha$  (2.77 KeV) and Ti  $K\beta$  (3.18 KeV). The theoretical intensity ratio of Th  $M\alpha$  to Th  $M\beta$  is 5:3. A peak at 2.34 KeV may be associated with S (S  $K\alpha$ ), while a peak at 3.7 KeV is assigned to Ca (Ca  $K\alpha$ ). STEM-EDS data for ALOOH phase with a diaspore structure, including a BF image and a SAED pattern as well as a STEM-EDS spectrum (e). The viewing direction for its SAED pattern is [100]. STEM-EDS data for Th-free clay-like phases, including a BF image and its Debye-Scherrer ring patterns as well as a STEM-EDS spectrum (f). A peak at 2.77 KeV is related to the Si escape peak for Ti  $K\alpha$ . The almost visible narrow peak of Na is due to background noise.

(see Supplementary Fig. S11c,d, respectively) have proved, along with the STEM-EDS spectra, the absence of Th in all studied anatase particles. The observed ALOOH polymorphs corresponding to diaspore ( $\alpha$ -ALOOH) contain Fe and Cr impurities (Fig. 4e). Moreover, Th-free clay-like phases (with major d-spacings corresponding to 0.31 nm, 0.28 nm, 0.26 nm and 0.17 nm; Fig. 4f) have also been confirmed as components in the “Al-Fe-Ca-Ti-Si-Na-Cr matrix”. The obtained Debye-Scherrer ring patterns of clay-like particles suggest that this phase could be related to a zeolite-type material, which is rather doubtful due to its unusual chemical composition (Si: 19.87 wt.%; Al: 10.71 wt.%; Ca: 10.94 wt.%; Ti: 20.63 wt.%; O: 37.81 wt.% as major elements and C, P and S as minor elements). We might also assume that this phase could be an admixture of several nano-phases. Iron and chromium peaks attributed to the presence of Ti-containing hematite crystallites, as these Fe-oxides, are often associated with clay-like phases and nano-perovskite into the “Al-Fe-Ca-Ti-Si-Na-Cr matrix” (Supplementary Fig. S12). Thus, the STEM-EDS/EELS study revealed that both the initial and acid-treated “Al-Fe-Ca-Ti-Si-Na-Cr matrix”, as appeared at the microscale, are actually an aggregate of several Al-, Fe-, Ca-, Ti-, Si-, Na-, Cr- (and also S-, P-, Ce-, Nb-, Zr-, and maybe, Sr-) particles, including the Th-hosting nano-perovskite. There is no evidence for other phases hosting Th, neither at the microscale (see text above) nor at the nanoscale, except for the nano-perovskite, but the minor presence of element traces, in isolated parts of various BR phases, might not be excluded.

**EXAFS spectroscopy and the local environment of Th.** Details on the structural characteristics of Th, assigned to the discovered low-T and low-P nano-perovskite ( $\text{Ca}_{0.8}\text{Na}_{0.2}\text{TiO}_3$ ), have been obtained by X-ray absorption fine structure spectroscopy/XAFS (Th  $L_{\text{III}}$ -edge XANES and, especially, EXAFS) spectra and data processing using the ATHENA<sup>54</sup> and EDA<sup>55</sup> software packages. The Th  $L_{\text{III}}$ -edge bulk XANES results of the studied BR, together with bulk & micro-XANES of Greek industrial bauxite<sup>27,28</sup> in comparison with spectra of reference materials indicated that the valence of Th is typical 4+ (Supplementary Fig. S13). The experimental Th  $L_{\text{III}}$ -edge EXAFS spectrum of the BR, which was measured in the fluorescence mode, is noisy above  $k = 6 \text{ \AA}^{-1}$  (Supplementary Fig. S14). This fact limits the accuracy of the analysis, as well as it reduces its resolution in the R-space. The EXAFS spectrum does not show any evidence for significant high frequency contributions either. This fact is compatible with the shape of the EXAFS spectrum Fourier transform (Supplementary Figure S14), which consists of a single broad peak located at 1.6 Å. Thus, the contribution of outer coordination shells around thorium is smeared out, and only analysis of the nearest environment can be performed. The first peak contribution into the total EXAFS spectrum was singled out by the Fourier filtering procedure and best fitted using two different approaches: the one-component Gaussian model<sup>56</sup> and the regularization method<sup>57</sup>. It is considerable that in the latter method, the radial distribution function (RDF) could have had an arbitrary shape and, thus, may possibly account for anharmonicity and strong disorder effects. In both models, the theoretical backscattering amplitude and phases shift functions for the Th-O atom pair were calculated by the *ab initio* real-space FEFF8 code<sup>58</sup>, employing a complex Hedin-Lundqvist exchange-correlation potentially accounting for inelastic effects. The results of the best fits, obtained within the two models (i.e., Gaussian and regularization method) in the k-space range from 2 to 6 Å<sup>-1</sup>, are shown in the upper and middle images of Fig. 5, respectively, and the corresponding RDF's of them are given in the lower image of Fig. 5. The regularization method results in better agreement, suggesting a deviation of the RDF shape from the Gaussian form. The numerical values of structural parameters for both models are given in Table 1. For the sake of discussion, it is noteworthy that, due to the short k-range interval of the EXAFS spectrum, there is a strong correlation between the values of the coordination number N and the Debye-Waller factor  $\sigma^2$ . The local environment of Th ions in the studied BR is not very far from that in Fe-depleted bauxite<sup>27,28</sup>, but is significantly more disordered as is evidenced by the larger value of Debye-Waller factor in the Gaussian model and broad RDF's in Fig. 5. As in the case of Fe-depleted bauxite<sup>27,28</sup> the Th ions in BR are coordinated by about 7–8 oxygen atoms. This coordination number of Th is smaller than that in Th-nitrate (N = 12), being in agreement with the difference in the mean Th-O distances. However, it is notable that in the case of bauxite, being the basic parent material of BR, Th is hosted in microscale anatase (TiO<sub>2</sub> polymorph) and there is no evidence for any perovskite phase. It is known that Th<sup>4+</sup> in the structure of CaSiO<sub>3</sub> perovskite, synthesized at high temperature (and occasionally at high pressure), may fundamentally occupy “large” Ca dodecahedral sites (<sup>12</sup>Ca<sup>2+</sup>) or “small” Si octahedral sites (<sup>6</sup>Si<sup>4+</sup>)<sup>59</sup>. On the other hand, in the structure of CaTiO<sub>3</sub> perovskite<sup>60</sup> Ti appears as <sup>6</sup>Ti<sup>4+</sup>, whereas Ca may be <sup>8</sup>Ca<sup>2+</sup> or even <sup>7</sup>Ca<sup>2+</sup>, compared to <sup>12</sup>Ca<sup>2+</sup> in the ideal perovskite structure. As one can see in the lower image of Fig. 5, the distribution of the Ca-O distances in CaTiO<sub>3</sub> perovskite agrees well with the shape of the Th-O RDF in BR, obtained by the regularization method. Consequently, the Th  $L_{\text{III}}$ -edge EXAFS signal was simulated by the FEFF8 code for the case of Th-absorbing atom substituting calcium or titanium in CaTiO<sub>3</sub> perovskite. The calculated Th  $L_{\text{III}}$ -edge EXAFS signals are compared with the experimental one for BR; see upper image of Fig. 6). In the frame of this simulation, the atom positions were fixed as in orthorhombic CaTiO<sub>3</sub> perovskite-type structure<sup>60</sup>, and all Debye-Waller factors were set to zero

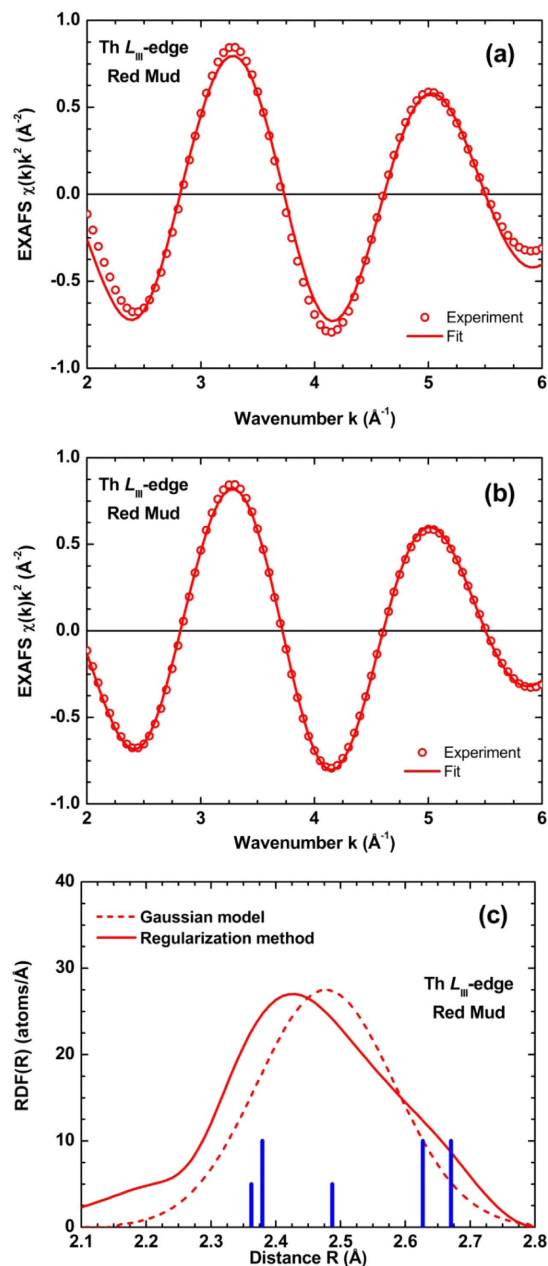


**Figure 5.** Best-fit results for the first shell Th  $L_{III}$ -edge EXAFS in the Greek bauxite residue/BR (red mud) using the one-shell Gaussian model (a), and the regularization method (b). Comparison of the radial distribution functions (RDF's), obtained from the first shell Th  $L_{III}$ -edge EXAFS (c) using the one-shell Gaussian model (dashed line) and the regularization method (solid line). The blue bars indicate the position of the Ca-O distances in  $\text{CaTiO}_3$  perovskite<sup>60</sup>.

that explains smaller damping of the calculated EXAFS amplitude at larger  $k$ -values. As one can see (upper image of Fig. 6), the model of Th at the Ca site ( $\text{Ca}(\text{Th})\text{TiO}_3$ ) results in the overall amplitude and main frequency of the EXAFS signal close to the experimental one, whereas the model of Th at the Ti site ( $\text{CaTi}(\text{Th})\text{O}_3$ ) differs from the experiment significantly, in both amplitude and frequency. Unfortunately, the weak contribution of the outer shells (Supplementary Fig. S14) in the experimental Th  $L_{III}$ -edge EXAFS spectrum in BR does not allow us to make unambiguous conclusion on the Th location. However, taking into account the above argument about Th in Ca site of the nano-perovskite, in conjunction with the best-fit EXAFS results ( $R = 2.42$ – $2.48$  Å and  $\text{CN} = 7$ – $8$ ), we could presume that Th, hosted in the low-T and low-P novel Ca-Na-(Ce-Nb-Zr-Cr)-nano-perovskite of the studied BR, occupies  $\text{Ca}^{2+}$  sites rather than  $\text{Ti}^{4+}$  sites (lower image of Fig. 6).

**Environmental and technological implications about the Greek bauxite residue (red mud).** It is herein stated that the novel low-T and low-P Th-hosting Ca-Na-(Ce-Nb-Zr-Cr)-nano-perovskite ( $\text{Ca}_{0.8}\text{Na}_{0.2}\text{TiO}_3$ ) is the reason of the low Th release in acid medium, and subsequently of the Th immobility if the Greek bauxite

	Greek Red Mud (present study) Th $L_{III}$ -edge bulk- EXAFS	Greek Bauxite <sup>27,28</sup>	
		Th $L_{III}$ -edge bulk-EXAFS	Th $L_{III}$ -edge Micro-EXAFS
<i>Gaussian model</i>			
CN $\pm$ 0.7	7.3	6.9	6.9
R ( $\text{\AA}$ ) $\pm$ 0.04	2.48	2.46	2.45
$\sigma^2$ ( $\text{\AA}^2$ ) $\pm$ 0.002	0.011	0.007	0.006
<i>Regularization method</i>			
CN	8.0	7.4	7.4
R ( $\text{\AA}$ )	2.42	2.40	2.38

**Table 1.** Th structural parameters for the studied Greek bauxite residue/BR (red mud), in comparison with the Greek bauxite values<sup>27,28</sup>, obtained from the processing of the EXAFS signals using the EDA software package<sup>55</sup>. \*This distance is the position of the RDF maximum.

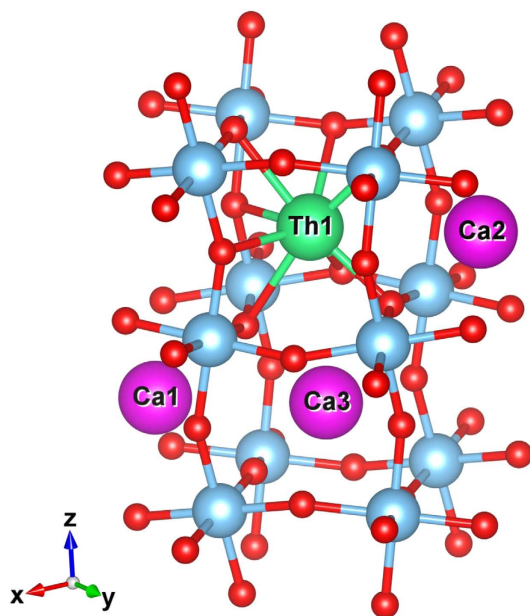
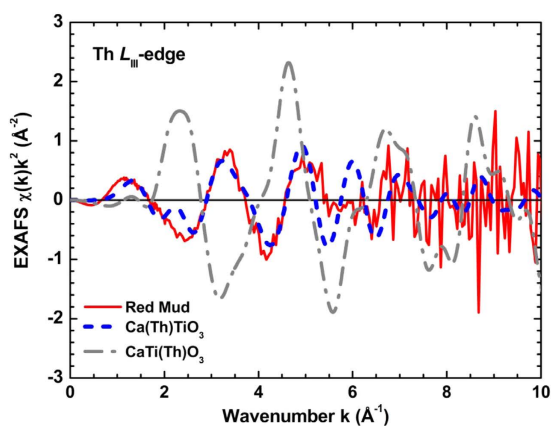


**Figure 6.** *Upper image:* The experimental (red solid line) and the calculated (blue dashed line: Th at the Ca site; grey dash-dotted line: Th at the Ti site) Th  $L_{III}$ -edge EXAFS spectra of the studied Greek bauxite residue/BR (red mud) and Th-substituted CaTiO<sub>3</sub> perovskite, respectively; *Lower image:* The structure of orthorhombic CaTiO<sub>3</sub> perovskite<sup>60</sup> with Th substituting Ca. Oxygen, titanium, and calcium atoms are illustrated by red-, blue-, and magenta-colored balls, respectively, whereas the thorium atom is indicated by green-colored ball.

residue/BR (i.e., red mud) is exposed to Mediterranean seawater. In general, it is demonstrated that Greek BR, and perhaps huge quantities of BR around the world, do not constitute, under certain circumstances an environmental hazard due to actinide content and radioactivity. In turn, BR is a valuable alumina refineries' by-product to be used as secondary resource for a sustainable supply of critical & strategic elements (such as REEs) and, thus contribute to a more sustainable "modus operandi".

## Conclusions

The nature of thorium in the bauxite residue/BR (the so-called "red mud") from Greek Al industry has been investigated in detail for the first time in the literature. The interest arises from the fact that huge quantities of that BR, showing relative radioactivity, had been deposited into the Mediterranean Sea in Greece. The chemical analysis and the HR  $\gamma$ -ray measurements proved that the observed higher radioactivity is higher compared to the parent Greek bauxite, mainly attributed to the presence of Th ( $111 \mu\text{g g}^{-1}$ ;  $355 \text{Bq kg}^{-1}$  for  $^{232}\text{Th}$ ). The marine environment might not be affected by this actinide element; leaching experiments have confirmed negligible Th release in Mediterranean seawater, at least after 12 months of interaction. In contrast, the experiments of the present study indicated that the mobility of V might be of potential risk. Characterizing the studied BR in microscale yielded no evidence of Th hosting phase into a homogeneous "Al-Fe-Ca-Ti-Si-Na-Cr matrix. However, the STEM study of the leached BR sample at the nanoscale showed that the immobility of Th can be attributed to the existence of an insoluble nano-perovskite with major composition of  $\text{Ca}_{0.8}\text{Na}_{0.2}\text{TiO}_3$ . Subsequent study of Th  $L_{\text{III}}$ -edge EXAFS spectroscopy revealed that the local environment of  $\text{Th}^{4+}$  in the structure of nano-perovskite is occupying  $\text{Ca}^{2+}$  sites, rather than  $\text{Ti}^{4+}$  sites. We do consider that this structural peculiarity is related to the negligible Th release in the Mediterranean seawater.

## Materials and Methods

### Samples and Initial Characterization (PXRD, WDXRF, ICP-OES/MS, HR $\gamma$ -ray spectroscopy).

The BR samples were supplied by the "Aluminium of Greece S.A." alumina plant at Agios Nikolaos (Antikyra, Gulf of Corinth, central Greece). The WDXRF measurements for the major and trace elements of BR were performed on a PANalytical AxiosmAX WDXRF spectrometer using the Pro - Trace measurement and analysis application package at the PANalytical B.V. laboratories. For more details about the samples and about the characterization techniques, please consult the Supplementary Information.

### Seawater and Acid-Leaching Experiments (SF-ICP-MS).

Leaching experiments on the investigated BR and bauxite samples were carried out using (a) Mediterranean seawater from the Gulf of Corinth (Greece), and (b) concentrated acetic acid (Merck), over a period ranged from 2 weeks to 1 year. Acetic acid was used, instead of typical TCLP, according to a recent relevant work on red mud<sup>31</sup>. The analyses of leachates for potentially hazardous metals and metalloids (Cr, V, Ni, As, Pb), Th, Ta, Nb, and REE, were performed using a SF-ICP-MS (Thermo Scientific Element 2/XR). For more details, please consult the Supplementary Information and the Supplementary Tables S1 and S2.

### Electron Microscopy (SEM-EDS, STEM-EDS/EELS and STEM-HAADF).

Details on the elemental composition of BR were obtained on carbon-coated free surfaces and polished (in epoxy resin) solid samples using a Jeol JSM-5600 SEM equipped with an Oxford EDS. The observations were made with an accelerating voltage of 20 kV, a working distance of 20 mm, a current beam of 1.5 nA, an active time of 20–100 s and a magnification from  $\times 35$  to  $\times 3500$ . Pure metallic materials and minerals were used as standards. STEM-EDS/EELS and STEM-HAADF were carried out using an FEI probe-corrected Titan 80-300ST FEG TEM, equipped with an Oxford Instrument X-Max 80 mm<sup>2</sup> silicon drift detector and a Gatan Tridium imaging filter. SAED was used to identify mineral phases. For the detection of Th, we performed TEM-EDS with count rates of 5,000–8,000 counts  $\text{sec}^{-1}$  and dwell times of 60–180 sec (i.e., at total counts of 500,000–700,000), using a Gatan low-background Be specimen holder. The EELS measurements were made in TEM diffraction mode with an energy resolution of 0.9 eV.

### X-ray Absorption Fine Structure Spectroscopy (XAFS).

Bulk XAFS (EXAFS/XANES) spectroscopic study of BR was performed at the Th  $L_{\text{III}}$ -edge (16300 eV; energy was calibrated using a Y metal foil) in the fluorescence mode on powdered samples pressed with cellulose into pellets. Spectra were obtained at the SUL-X beamline of the ANKA Synchrotron Radiation Facility (KIT, Germany). Thorium compounds ( $\text{Th}(\text{NO}_3)_4 \cdot 4\text{H}_2\text{O}$  and  $\text{ThO}_2$ ) and minerals containing Th impurities, such as zircon ( $\text{ZrSiO}_4$ ), were used as reference materials. The XAFS spectra were analyzed using the ATHENA<sup>54</sup> and the EDAS<sup>55</sup> software packages. The EXAFS signal corresponding to the first main peak in Fourier transforms (FTs) was isolated using the Fourier filtering procedure. The range of the back-FT was 1–3 Å for  $\text{Th}(\text{NO}_3)_4 \cdot 4\text{H}_2\text{O}$  and 0.8–2.5 Å for the samples. Thus, obtained EXAFS signals were simulated using two different approaches: the conventional Gaussian model<sup>56</sup> and the regularization method<sup>57</sup>. The theoretical backscattering amplitude and phase shift functions for Th-O atom pair were calculated by the *ab initio* FEFF8 code<sup>58</sup> using a complex Hedin-Lundqvist exchange-correlation potential accounting for inelastic effects.

## References

- Burke, I. T. *et al.* Behavior of aluminum, arsenic, and vanadium during the neutralization of red mud leachate by HCl, gypsum, or seawater. *Environ. Sci. Technol.* **47**, 6527–6535 (2013).
- Liang, W. *et al.* Effect of strong acids on red mud structural and fluoride adsorption properties. *J. Colloid Interf. Sci.* **423**, 158–165 (2014).
- Borra, C. R., Pontikes, Y., Binnemans, K. & Van Gerven, T. Leaching of rare earths from bauxite residue (red mud). *Min. Engineer.* **76**, 20–27 (2015).

4. Borra, C. R., Blanpain, B., Pontikes, Y., Binnemans, K. & Van Gerven, T. Smelting of bauxite residue (red mud) in view of iron and Selective rare earths recovery. *J. Sustain. Metall.* 1–10 (2015).
5. Schiermeier, Q. & Balling, Y. *Analysis lags on Hungarian sludge leak*. Nature News. (2010) Available at: <http://www.nature.com/news/2010/101011/full/news.2010.531.html>. (Accessed: 11<sup>th</sup> October 2010).
6. Enserink, M. After red mud flood, scientists try to halt wave of fear and rumors. *Science* **330**, 432–433 (2010).
7. Burke, I. T. *et al.* Speciation of arsenic, chromium, and vanadium in red mud samples from the Ajka spill site, Hungary. *Environ. Sci. Technol.* **46**, 3085–3092 (2012).
8. Ruyters, S. *et al.* The red mud accident in Ajka (Hungary): plant toxicity and trace metal bioavailability in red mud contaminated soil. *Environ. Sci. Technol.* **45**, 1616–1622 (2011).
9. Vavadakis, D., Agioutantis, Z., Xenidis, A. & Boufounos, D. Simulation of bauxite residues disposal in abandoned mine open pits. Paper presented at: The 2<sup>nd</sup> International Conference on: Advances in Mineral Resources Management and Environmental Geotechnology (AMIREG 2006), Hania, Crete, Greece. Santorini: Heliotopos Conferences. (2006, September 25–27).
10. Agatzini-Leonardou, S., Oustadakis, P., Tsakiridis, P. E. & Markopoulos, Ch. Titanium leaching from red mud by diluted sulfuric acid at atmospheric pressure. *J. Hazard. Mater.* **157**, 579–586 (2008).
11. Pontikes, Y., Vangelatos, I., Boufounos, D., Fafoutis, D. & Angelopoulos, G. N. Environmental aspects on the use of Bayer's process bauxite residue in the production of ceramics. Paper presented at: The 11<sup>th</sup> International Ceramics Congress, Sicily, Italy. Switzerland: Trans Tech Publications. (doi: 10.4028/www.scientific.net/AST.45.2176) (2006, June 4–9).
12. Pontikes, Y. Utilization of red mud in the heavy clay industry. Ph.D. Thesis, University of Patras, Greece, 2007.
13. Pontikes, Y. & Angelopoulos, G. Bauxite residue in cement and cementitious applications: Current status and a possible way forward. *Resour. Conserv. Recy.* **73**, 53–63 (2013).
14. Varnavas, S., Ferentinos, G. & Collins, M. Dispersion of bauxitic red mud in the Gulf of Corinth, Greece. *Mar. Geol.* **70**, 211–222 (1986).
15. Varnavas, S. & Achilleopoulos, P. P. Factors controlling the vertical and spatial transport of metal-rich particulate matter in seawater at the outfall of bauxitic red mud toxic waste. *Sci. Total Environ.* **175**, 199–205 (1995).
16. Papatheodorou, G., Papaefthymiou, H., Maratou, A. & Ferentinos, G. Natural radionuclides in bauxitic tailings (red-mud) in the Gulf of Corinth, Greece. *Radioprotection* **40**, 549–555 (2005).
17. Karagiannidi, Th., Papaefthymiou, H. & Papatheodorou, G. Radioactive impact of a bauxite beneficiation plant in the Itea Gulf (Gulf of Corinth, Greece). *J. Radioanal. Nucl. Ch.* **279**, 923–934 (2009).
18. Samouhos, M., Taxiarchou, M., Tsakiridis, P. E. & Potiriadis, K. Greek “red mud” residue: A study of microwave reductive roasting followed by magnetic separation for a metallic iron recovery process. *J. Hazard. Mater.* **254–255**, 193–205 (2013).
19. Balomenos, E., Kastritis, D., Panias, D., Paspaliaris, I. & Boufounos, D. The ENEXAL bauxite residue treatment process: industrial scale pilot plant results. Paper presented at The TMS (The Minerals, Metals & Materials Society: TMS 2014 143<sup>rd</sup> Annual Meeting & Exhibition, San Diego, California, USA. Hoboken, NJ, USA: Light Metals, John Wiley & Sons. (doi: 10.1002/9781118888438.ch25) (2014, February 16–20).
20. Binnemans, K., Jones, P. T., Blanpain, B., Gerven, T. V. & Pontikes, Y. Towards zero-waste valorisation of rare-earth-containing industrial process residues: a critical review. *J. Clean. Prod.* **99**, 17–38 (2015).
21. Ochsenkühn-Petropulu, M., Lyberopulu, Th. & Parissakis, G. Direct determination of lanthanides, yttrium and scandium in bauxites and red mud from alumina production. *An. Chim. Acta* **296**, 305–313 (1994).
22. Lympelopoulou, Th. Determination and recovery of rare earth elements from bauxites and red mud. Ph.D. Thesis, National Technical University of Athens, Greece (1996).
23. Ochsenkühn-Petropulu, M., Lyberopulu, Th., Ochsenkühn, K. M. & Parissakis, G. Recovery of lanthanides and yttrium from red mud by selective leaching. *An. Chim. Acta* **319**, 249–254 (1996).
24. Ochsenkühn-Petropoulou, M. Th., Hatzilyberis, K. S., Mendrinos, L. N. & Salmas, C. E. Pilot-plant investigation of the leaching process for the recovery of scandium from red mud. *Ind. Eng. Chem. Res.* **41**, 5794–5801 (2002).
25. Ochsenkühn-Petropulu, M., Lyberopulu, Th. & Parissakis, G. Selective separation and determination of scandium from yttrium and lanthanides in red mud by a combined ion exchange/solvent extraction method. *An. Chim. Acta* **315**, 231–237 (1995).
26. Tsakanika, L. V., Ochsenkühn-Petropoulou, M. Th. & Mendrinos, L. N. Investigation of the separation of scandium and rare earth elements from red mud by use of reversed-phase HPLC. *Anal. Bioanal. Chem.* **379**, 796–802 (2004).
27. Gamaletsos, P. *et al.* Thorium partitioning in Greek industrial bauxite investigated by synchrotron radiation and laser-ablation techniques. *Nucl. Instrum. Meth. B.* **269**, 3067–3073 (2011).
28. Gamaletsos, P. Mineralogy and geochemistry of bauxites from Parnassos-Ghiona mines and the impact on the origin of the deposits. Ph.D. Thesis, University of Athens, Greece (2014).
29. Gu, H. & Wang, N. Leaching of uranium and thorium from red mud using sequential extraction methods. *Fresen. Environ. Bull.* **22**, 2763–2769 (2013).
30. Tessier, A., Campbel, P. G. C. & Bisson, M. Sequential extraction procedure for the speciation of particulate trace metals. *Anal. Chem.* **51**, 844–851 (1979).
31. Rubinos, D. A. & Barral, M. T. Fractionation and mobility of metals in bauxite red mud. *Environ. Sci. Pollut. Res.* **20**, 7787–7802 (2013).
32. Sato, C., Kazama, S., Sakamoto, A. & Hirayanagi, K. Behavior of radioactive elements (uranium and thorium) in Bayer process. Paper presented at the Technical Sessions Sponsored by the Tms Light Metal (Sic) Committee at 115<sup>th</sup> Annual Meeting, New Orleans, Louisiana. Hoboken, NJ, USA: Light Metals, John Wiley & Sons (doi: 10.1002/9781118647868.ch25) (1986, March 2–6).
33. Qu, Y. & Lian, B. Bioleaching of rare earth and radioactive elements from red mud using *Penicillium tricolor* RM-10. *Biores. Technol.* **136**, 16–23 (2013).
34. Collins, R. N., Clark, M. W. & Payne, T. E. Solid phases responsible for Mn<sup>II</sup>, Cr<sup>III</sup>, Co<sup>II</sup>, Ni, Cu<sup>II</sup> and Zn immobilization by a modified bauxite refinery residue (red mud) at pH 7.5. *Chem. Engineer. J.* **236**, 419–429 (2014).
35. Binnemans, K. & Jones, P. T. Rare earths and the balance problem. *J. Sustain. Metall.* **1**, 29–38 (2015).
36. Bian, Z. *et al.* The challenges of reusing mining and mineral-processing wastes. *Science* **337**, 702–703 (2012).
37. Liu, G., Bangs, C. E. & Müller, D. B. Unearthing potentials for decarbonizing the U.S. aluminum cycle. *Environ. Sci. Technol.* **45**, 9515–9522 (2011).
38. Liu, G. & Müller D. B. Mapping the global journey of anthropogenic aluminum: A trade-linked multilevel material flow analysis. *Environ. Sci. Technol.* **47**, 11873–11881 (2013).
39. Liu, Y. & Naidu, R. Hidden values in bauxite residue (red mud): Recovery of metals. *Waste Manage.* **34**, 2662–2673 (2014).
40. Li, Y. -H. Distribution patterns of the elements in the ocean: a synthesis. *Geochim. Cosmochim. Acta* **55**, 3223–3240 (1991).
41. Gräfe, M. *et al.* Combined application of QEM-SEM and hard X-ray microscopy to determine mineralogical associations and chemical speciation of trace metals. *J. Environ. Quality* **40**, 767–783 (2011).
42. Alonso, E. *et al.* Evaluating Rare Earth Element Availability: A Case with revolutionary demand from clean technologies. *Environ. Sci. Technol.* **46**, 3406–3414 (2012).
43. Gräfe, M., Power, G. & Klauber, C. Bauxite residue issues: III. Alkalinity and associated chemistry. *Hydrometall.* **108**, 60–79 (2011).
44. Liu, Y., Lin, C. & Wu, Y. Characterization of red mud derived from a combined Bayer process and bauxite calcination method. *J. Hazard. Mater.* **146**, 255–261 (2007).

45. Atasoy, A. An investigation on characterization and thermal analysis of the Aughinish red mud. *J. Therm. Anal. Calorim.* **81**, 357–361 (2005).
46. Atasoy, A. The comparison of the Bayer process wastes on the base of chemical and physical properties. *J. Therm. Anal. Calorim.* **90**, 153–158 (2007).
47. Venugopalan, T. A., Sharma, J. M. & Prasad, P. M. Utilisation of red mud in India. Paper presented at The International Conference on Bauxite Tailings, Kingston, Jamaica. Jamaica: Jamaica Bauxite Institute. (1986, October 26–31).
48. Santini, T. C. Application of the Rietveld refinement method for quantification of mineral concentrations in bauxite residues (alumina refining tailings). *Int. J. Miner. Process.* **139**, 1–10 (2015).
49. Gu, H., Wang, N. & Liu, S. Characterization of Bayer red mud from Guizhou, China. *Min. Metall. Process.* **29**, 169–171 (2012).
50. Connelly, N. G., Damhus, T., Hartshorn, R. M. & Hutton, A. T. Nomenclature of inorganic chemistry: IUPAC Recommendations 2005, 1st edn (eds Connelly, N. G. & Damhus, T.), published for the International Union of Pure and Applied Chemistry, The Royal Society of Chemistry [ISBN 0-85404-438-8] (RSC Publishing, 2005).
51. Tubchareon, T., Soisuwan, S., Ratanathammaphan, S. & Praserttham, P. Effect of Na-, K-, Mg, and Ga dopants in A/B-sites on the optical band gap and photoluminescence behavior of  $[\text{Ba}_{0.5}\text{Sr}_{0.5}]\text{TiO}_3$  powders. *J. Lumin.* **142**, 75–80 (2013).
52. Tubchareon, T., Soisuwan, S., Ratanathammaphan, S. & Praserttham, P. Effect of Na content on the physical properties of  $\text{Ba}_{0.5}\text{Sr}_{0.5}\text{TiO}_3$  powders. *Adv. Mater. Sci. Eng.* 2014 Article ID **602504**, 1–7 (2014).
53. Seki, H., Yamada, R., Saito, T., Kennedy, B. & Shimakawa, Y. High-concentration Na doping of  $\text{SrRuO}_3$  and  $\text{CaRuO}_3$ . *Inorg. Chem.* **53**, 4579–4584 (2014).
54. Ravel, B. & Newville, M. ATHENA, ARTEMIS, HEPHAESTUS: data analysis for X-ray absorption spectroscopy using IFEFFIT. *J. Synchrotron Radiat.* **12**, 537–541 (2005).
55. Kuzmin, A. EDA: EXAFS data analysis software package. *Physica B* **208–209**, 175–176 (1995).
56. Aksenov, V. L., Kovalchuk, M. V., Kuzmin, A. Yu., Purans, Yu. & Tyutyunnikov, S. I. Development of methods of EXAFS spectroscopy on Synchrotron radiation beam: Review. *Crystallogr. Rep.* **51**, 908–935 (2006).
57. Kuzmin, A. & Purans, J. Dehydration of the molybdenum trioxide hydrates  $\text{MoO}_3 \cdot n\text{H}_2\text{O}$ : *in situ* x-ray absorption spectroscopy study at the Mo K edge. *J. Phys.: Condens. Matter.* **12**, 1959–1970 (2000).
58. Ankudinov, A. L., Ravel, B., Rehr, J. J. & Conradson, S. D. Real-space multiple-scattering calculation and interpretation of x-ray-absorption near-edge structure. *Phys. Rev. B* **58**, 7565–7576 (1998).
59. Gréaux, S. *et al.* X-ray absorption near edge structure (XANES) study of the speciation of uranium and thorium in Al-rich  $\text{CaSiO}_3$  perovskite. *Am. Mineral.* **97**, 100–109 (2012).
60. Buttner, R. H. & Maslen, E. N. Structural parameters and electron difference density in  $\text{BaTiO}_3$ . *Acta Cryst. B* **48**, 764–796 (1992).

## Acknowledgements

“Aluminium of Greece S.A.,” “S&B Industrial Minerals S.A.” and “ELMIN S.A.” are acknowledged for the provision of bauxite residue and bauxite samples. We are grateful to Mr G. Georgalas, Mr D. Kosmetatos, Mr A. Delipaltas and Dr V. Vassiliadou, for comments and authorizing the present publication, as well as Mr G. Delimichalis for his assistance in Pera-Lakkos underground mine. We are thankful to Ms Berit Wenzell from the Center for Electron Nanoscopy (CEN) of the Technical University of Denmark (DTU) for collaboration during the SEM-EDS measurements. A.P. Møller and Chastine Mc-Kinney Møller Foundation are gratefully acknowledged for their contribution toward the establishment of the DTU CEN. We also acknowledge the ANKA Synchrotron Radiation Facility/KIT (Karlsruhe, Germany) for providing beamtime at the SUL-X beamline. Finally, we would like to thank Professor Sofoklis Makridis, Editor in Scientific Reports of NPG, for his invitation to publish our investigation in this journal.

## Author Contributions

P.N.G., A.G., T.K., Y.P. and G.N.A. designed and organized research; P.N.G., A.G., S.X., C.Z., A.Ko., E.T. and A.F. performed the bulk and microscale characterization; P.N.G. and M.L. performed the seawater and acid-leaching experiments; P.N.G. and T.K. performed the nanoscale characterization; P.N.G., A.G., A.Ku., T.J.M., J.G. and R.S. undertook the XAFS study; P.N.G. and A.G. wrote the paper; all authors contributed to interpretation of the results and editing of the manuscript.

## Additional Information

**Supplementary information** accompanies this paper at <http://www.nature.com/srep>

**Competing financial interests:** The authors declare no competing financial interests.

**How to cite this article:** Gamaletsos, P. N. *et al.* The role of nano-perovskite in the negligible thorium release in seawater from Greek bauxite residue (red mud). *Sci. Rep.* **6**, 21737; doi: 10.1038/srep21737 (2016).



This work is licensed under a Creative Commons Attribution 4.0 International License. The images or other third party material in this article are included in the article’s Creative Commons license, unless indicated otherwise in the credit line; if the material is not included under the Creative Commons license, users will need to obtain permission from the license holder to reproduce the material. To view a copy of this license, visit <http://creativecommons.org/licenses/by/4.0/>

## **Supplementary Information**

### **The role of nano-perovskite in the negligible thorium release in seawater from Greek bauxite residue (red mud)**

Platon N. Gamaletsos<sup>1,2,6,\*</sup>, Athanasios Godelitsas<sup>2</sup>, Takeshi Kasama<sup>1</sup>, Alexei Kuzmin<sup>3</sup>, Markus Lagos<sup>4</sup>,  
Theo J. Mertzimekis<sup>5</sup>, Jörg Göttlicher<sup>6</sup>, Ralph Steininger<sup>6</sup>, Stelios Xanthos<sup>7,8</sup>, Yiannis Pontikes<sup>9</sup>, George  
N. Angelopoulos<sup>10</sup>, Charalampos Zarkadas<sup>11</sup>, Aleksandr Komelkov<sup>11</sup>, Evangelos Tzamos<sup>12</sup> and Anestis  
Filippidis<sup>12</sup>

<sup>1</sup> Center for Electron Nanoscopy, Technical University of Denmark, 2800 Kongens Lyngby, Denmark

<sup>2</sup> Faculty of Geology & Geoenvironment, National and Kapodistrian University of Athens, Zografou Campus, 15784 Athens,  
Greece

<sup>3</sup> Institute of Solid State Physics, University of Latvia, Kengaraga str. 8, 1063 Riga, Latvia

<sup>4</sup> Karlsruhe Institute of Technology, Institute for Nuclear Waste Disposal, Hermann-von-Helmholtz-Platz 1, 76344  
Eggenstein-Leopoldshafen, Germany

<sup>5</sup> Faculty of Physics, National and Kapodistrian University of Athens, Zografou Campus, 15784 Athens, Greece

<sup>6</sup> Karlsruhe Institute of Technology, ANKA Synchrotron Radiation Facility, Hermann-von-Helmholtz-Platz 1, 76344  
Eggenstein-Leopoldshafen, Germany

<sup>7</sup> Department of Electrical and Computer Engineering, Nuclear Technology Laboratory, Aristotle University of Thessaloniki,  
54124 Thessaloniki, Greece

<sup>8</sup> Department of Automation Engineering, Alexander Technological Educational Institute of Thessaloniki, 57400  
Thessaloniki, Greece

<sup>9</sup> KU Leuven, Department of Materials Engineering, Kasteelpark Arenberg 44, 3001 Leuven, Belgium

<sup>10</sup> University of Patras, Department of Chemical Engineering, 26500 Rio, Greece

<sup>11</sup> PANalytical B.V., 7600 AA Almelo, The Netherlands

<sup>12</sup> School of Geology, Aristotle University of Thessaloniki, 54124, Thessaloniki, Greece

---

\* Corresponding author: Platon Gamaletsos ([plagka@dtu.dk](mailto:plagka@dtu.dk))

**This supplement contains:**

**1. Supplementary Figures (14)**

**2. Supplementary Tables (4)**

**3. Supplementary References (27)**

## Materials and Methods

**Samples.** The bauxite residue / BR (red mud) samples were supplied by the “Aluminium of Greece S.A.” alumina plant at Agios Nikolaos (Antikyra, Gulf of Corinth, central Greece). The Company manages BR through the installation of four filter presses, disposing its final dewatered metallurgical residue (so-called “red mud”) onto a special configured area inside its plant. The bauxite residue, used in this study, consisted of composite sample, which was created by taking the appropriate number of specimens ( $n=10$ ) and using standard mixing procedures and sample splitters. Moreover, basic parent material (bauxite) samples ( $n=16$ ), used in the present study for reasons of comparison, were collected from underground mining sites at the Parnassos-Ghiona, which is an active mining area of the three Greek mining companies (“Aluminium of Greece S.A.” and its subsidiary “Delphi-Distomon S.A.”, “S&B Industrial Minerals S.A.” that has been recently consolidated by “Imerys S.A.”, and “ELMIN Hellenic Mining Enterprises S.A.”), exploiting bauxite from the Parnassos-Ghiona area (Central Greece). Greek industrial bauxites actually represent the typical low-grade (i.e., Fe-rich; diasporic & boehmitic; red-brown in color) and the high-grade (i.e., Fe-depleted; diasporic; white-grey in color) exploitable samples. It is worth noting that, except for Greek karst-type bauxite, which is the major part of the parent material that “Aluminium of Greece S.A.” uses at its industrial plant, the company also imports a small proportion of tropic bauxite for its needs, in order to be used as a mixture of Al-ores for its alumina production. On this basis, since the major part of parent material does consist of Greek bauxites, we strongly claim that karst-type bauxites from Parnassos-Ghiona active mining area represent the basic parent material of the present work.

**Powder X-ray Diffraction (PXRD) and Bulk Chemical Analyses (WDXRF and ICP-OES/MS).** The PXRD characterization of the raw, seawater-leached and acetic acid-leached BR sample was carried out using a Siemens D5005 (currently Bruker AXS) diffractometer with  $\text{CuK}\alpha$  radiation ( $\lambda = 1.54 \text{ \AA}$ ) at an accelerating voltage of 40 kV. Along with the major and trace element chemical analysis that were performed at the PANalytical B.V. laboratories (using a PANalytical Axios<sup>max</sup> WDXRF spectrometer), complementary analyses were also performed using a Perkin Elmer ICP-OES and a Perkin Elmer Sciex Elan 9000 ICP-MS spectrometer following a  $\text{LiBO}_2/\text{LiB}_4\text{O}_7$  fusion and  $\text{HNO}_3$  digestion of a 0.2 g sample. In addition, a separate 0.5 g split was digested in a  $\text{HNO}_3:\text{HCl}$  mixture (1:3) and analyzed by ICP-MS for precious and base metals.

**High-Resolution (HR) Gamma-Ray Spectroscopy.** HR  $\gamma$ -ray spectra of BR and the bauxite samples were collected using a Canberra high-purity germanium (HPGe) detector. Spectra analysis resulted in the natural radioactivity levels and total dose rate.

**Seawater and Acid-Leaching Experiments (SF-ICP-MS).** The bauxite residue / BR (red mud) used in the leaching experiments is a composite sample which was created by taking the appropriate number of specimens ( $n=10$ ), using standard mixing procedures and sample splitters. Simultaneously, similar leaching tests on Greek industrial bauxites were also carried out for comparison. For this purpose, two composite samples were also created to be used at leaching experiments, too. The bauxite composited samples, which are obtained from bauxite mines of “Aluminium of Greece S.A.” and its subsidiary “Delphi-Distomon S.A.”, represent both the typical low-grade (i.e., Fe-rich; diasporic & boehmitic; red-brown in color) and high-grade (i.e., Fe-depleted; diasporic; white-grey in color) karst-type bauxites from the Parnassos-Ghiona active mining area (central Greece). On a first step, powder from the BR, as well as from both the karst-type of bauxites (typically between  $\sim 10$  and  $100$  mg; details are given in **Supplementary Table S1**) were weighted in zinser vials, which were then filled with  $20$  mL of the leaching solution (i.e., seawater or concentrated acetic acid). In addition, two experimental blank runs (only seawater and concentrated acetic acid) were also prepared in the same way using zinser vials filled with  $20$  mL of the particular solution. Sampling of the experimental, as well as the blank solutions, was performed at certain periods of time after the start of the leaching procedure (after 2 weeks, 1 month, 2 months, 3 months, 5 months, 7 months, 10 months, 12 months).  $1$  mL was taken from each vial and filtered with a syringe filter to remove particles.  $500$   $\mu$ L of the filtered leachate was then further diluted using  $2$  vol%  $\text{HNO}_3$  (prepared from concentrated Merck ultrapure  $\text{HNO}_3$  and deionized water with a resistance of  $18$  m $\Omega$ ) to a total of  $5$  mL. The concentrations of trace elements, including actinides, HFSE and REEs, in the leachates were determined using a SF-ICP-MS spectrometer (Thermo Scientific Element 2/XR). Lanthanides and As were measured in high resolution mode ( $m/\Delta m = 10,000$ ), whereas other elements such as Cr, and V were measured in medium resolution ( $m/\Delta m = 4,000$ ) or in case of Ta, Y, Th, and Pb in low-resolution mode ( $m/\Delta m = 300$ ). Rhodium was added to the solutions and used as an internal standard (final Rh concentration was  $1$  ng  $\text{g}^{-1}$ ). Plasma parameters and sample uptake conditions were optimized at the beginning of each instrumental session to achieve optimal signal stability and maximum sensitivity at low oxide ratios. Typical instrumental parameters and measured isotopes are listed in **Supplementary Table S2**. Calibrations were generally performed with adjusted solutions using acetic acid and Mediterranean seawater for matrix matching. The accuracy of the measurements was verified with various water reference materials (TM26.3 and SPS-SW1), which were also adjusted with Mediterranean seawater and acetic acid for matrix matching. Since the water reference materials are not certified for Ta a diluted matrix matched reference solution of BHVO-1 (rock reference standard material) was used. All certified values could be reproduced throughout the measurements except for Dy, which is therefore not listed in **Supplementary Table S2**. The analyzed reference material solutions yielded consistently higher Dy concentrations due to unidentified spectral interferences.

## Results and Discussion

**PXRD study.** According to the PXRD patterns (**Supplementary Fig. S1**) the investigated Greek BR contains hematite ( $\alpha\text{-Fe}_2\text{O}_3$ ), calcite ( $\text{CaCO}_3$ ), ALOOH polymorphs (gibbsite:  $\text{Al}(\text{OH})_3$ ; diaspore;  $\alpha\text{-AlOOH}$ ) as well as Na-Ca-Al-silicate-carbonate and Ca-Al-hydroxysilicate phases (cancrinite- and “hydrogarnet”-type phases). “Hydrogarnet” may correspond to katoite<sup>1</sup> ( $\text{Ca}_3\text{Al}_2(\text{SiO}_4)_{3-x}(\text{OH})_{4x}$ ,  $x=1.5\text{-}3.0$  or  $\{\text{Ca}_3\}[\text{Al}_2](\square_3)(\text{OH})_{12}$ ), on the basis of previous measurements<sup>2</sup>. It should be noted that the same crystalline phases have also been detected in BR from Ajka alumina plant accident<sup>3</sup>. The same phases have also been detected in the case of seawater-treated samples. On the other hand, carbonate minerals (at least calcite), and also Ca-Al-hydroxysilicate phases, are practically absent in BR samples leached with acetic acid solutions. There is also a severe decrease in the intensity of cancrinite ( $\text{Na}_6\text{Ca}_2\text{Al}_6\text{Si}_6\text{O}_{24}(\text{CO}_3)_2$ ) peaks, in accordance with previous observations for acid-treated BR, by Liang et al. (2014)<sup>4</sup>. Moreover, distinct peaks of anatase, quartz and phyllosilicates/clay-like phases are revealed in the PXRD patterns of the acetic-acid leached BR. Therefore, Fe-oxides, Ti-oxides, ALOOH-polymorphs and clay-like phases are resistant in seawater and acetic acid solutions<sup>4,5</sup>.

**EELS Measurements.** The Ti  $L_{2,3}$ , Ca  $L_{2,3}$  and O  $K$ -edge EEL spectral data (**Supplementary Fig. S9**) indicate that the phase found in Greek BR has rather similar spectral characteristics with CTO studied by Calvert et al. (2006)<sup>6</sup>. The comparison of the nano-perovskite Ti  $L_{2,3}$  and O  $K$ -edges with CTO phases from literature has revealed that the Ti  $L_{2,3}$ -edges show structural similarities in terms of the observed crystal field effects<sup>6</sup>. In particular, the Ti  $L_{2,3}$ -edges show a well defined crystal field splitting of both the  $L_3$  (A1 and A2 peaks) and  $L_2$  edges (B1 and B2 peaks), very similar to the splitting phenomenon for reference  $\text{CaTiO}_3$  perovskite phase<sup>6</sup>. On the other hand, the splitting of  $L_2$  edge, into the B1 and B2 peaks seems to be less well-defined than that of  $L_3$ . The splitting can be assigned to a slight distortion of the  $\text{TiO}_6$  octahedra from tilting, due to the presence of Ca and Na, and/or changes in the degree of covalence in Ti-O bonding in the studied phase. It can also be assumed that BR nano-perovskite contains only  $\text{Ti}^{4+}$ , having almost the same EEL spectrum to that of CTO from literature<sup>6</sup>. Furthermore, the O  $K$ -edges can be separated into the  $A_{\parallel}$  and  $A_{\perp}$  components, corresponding to the A peaks that commonly appear within the 5-6 eV above the edge threshold; this is followed by another B peak, corresponding thus to B peaks that usually appear 10 eV above the threshold. The difference is the small and narrow A2 peak, between the A1 and A\* peaks of Calvert's reference CTOs<sup>6</sup>, which is not obvious in our O  $K$ -edge spectrum, maybe due to the presence of the stronger  $A_{\parallel}$  component within a

few electron volt or due to poor signal-to-noise ratio in the spectrum. The broader  $A_{II}$  component of our novel CTO is close to the intensity of sharper  $A_I$  component, giving assumption of a higher energy-loss shoulder. The broad B peak resembles to that of  $A_{II}$  peak and does not show any splitting phenomenon, which agrees to that of Calvert's reference CTOs<sup>6</sup>. In general, the shape of the O  $K$ -edge spectrum is in agreement. Taking into account the above, one may say that A components of the O  $K$ -edge EEL spectrum are attributed to the hybridization of the O 2p with Ti and Ca 3d-like states, while the B peak is due to hybridization of O 2p with TM 4s- and continuum-like states, as mentioned for CTO phases<sup>6</sup>. Moreover, according to the Na  $K$ -edge EEL data, there is no doubt that our nanoperoovskite also contains Na, which has been previously confirmed by STEM-EDS spectra (**Fig. 3**) and, additionally, by the quantitative EDS elemental maps (see image **d** of **Fig. 3**). Furthermore, the absence of N (401 eV) was confirmed as well, which “artificially” has been detected at 452 eV by STEM-EDS (see image **b** of **Fig. 3**). Actually, this “artificial” EDS N peak is attributed to Ti  $L\alpha$ .

**Supplementary Table S1:** Details of leaching experiments with regard to the studied bauxite residue / BR (red mud) and Greek typical low grade (i.e., Fe-rich; diasporic and boehmitic; red-brown in color) and high grade (i.e., Fe-depleted; diasporic; white-grey in color) bauxite samples.

Starting Date	Treatment Solution	Bauxite residue (red mud) & bauxite samples		Sample Weight (mg)	Amount of Solution (mL)	
		Type	Code			
6.11.2012	Concentrated Acetic Acid	Red Mud	RM-AC-1	102.4	20	
6.11.2012			RM-AC-2	12.5	20	
6.11.2012		Greek Bauxite	High Grade	HGB-AC-1	99.1	20
6.11.2012				HGB-AC-2	11.8	20
6.11.2012			Low Grade	LGB-AC-1	104.2	20
6.11.2012				LGB-AC-2	9.2	20
6.11.2012	Mediterranean seawater (Gulf of Corinth – Greece)	Red Mud	RM-SW-1	98.9	20	
6.11.2012			RM-SW-2	18.7	20	
6.11.2012			RM-SW-3	9.1	20	
6.11.2012		Greek Bauxite	High Grade	HGB-SW-1	102.7	20
6.11.2012				HGB-SW-2	20.9	20
6.11.2012				HGB-SW-3	10.8	20
6.11.2012			Low Grade	LGB-SW-1	99.2	20
6.11.2012				LGB-SW-2	19.9	20
6.11.2012				LGB-SW-3	9.9	20

**Supplementary Table S2:** Instrumental parameters for SF-ICP-MS measurements.

<b><i>Instrumental settings</i></b>	
Forward Power (W)	1250
Cooling gas flow rate (L min <sup>-1</sup> )	16
Auxiliary gas flow rate (L min <sup>-1</sup> )	0.9
Sample gas flow rate (L min <sup>-1</sup> )	1.195
Cones	Nickel

<b><i>Sample introduction</i></b>	
Nebulizer	PFA micro-concentric
Spray chamber	PC <sup>3</sup> -System

<b><i>Data acquisition</i></b>	
Monitored masses	<sup>232</sup> Th, <sup>207</sup> Pb, <sup>208</sup> Pb, <sup>89</sup> Y, <sup>181</sup> Ta (low resolution mode) <sup>53</sup> Cr, <sup>51</sup> V, <sup>113</sup> Cd (medium resolution mode) <sup>139</sup> La, <sup>140</sup> Ce, <sup>141</sup> Pr, <sup>146</sup> Nd, <sup>149</sup> Sm, <sup>153</sup> Eu, <sup>158</sup> Gd, Dy, <sup>159</sup> Tb, <sup>165</sup> Ho, <sup>167</sup> Er, <sup>169</sup> Tm, <sup>173</sup> Yb, <sup>175</sup> Lu, <sup>75</sup> As (high resolution mode)

**Supplementary Table S3:** Major and trace element concentrations in the studied bauxite residue (BR) mainly according to the WDXRF and, complementary, to the ICP-OES/MS measurements. Commonly, the elements in the light REE (LREE) and heavy REE (HREE) groups are arbitrary defined<sup>7-9</sup>.

<b>Fe<sub>2</sub>O<sub>3</sub></b>	(wt.%)	41.27	<b>Cr</b>	( $\mu\text{g g}^{-1}$ )	2403	<b>Y</b>	( $\mu\text{g g}^{-1}$ )	97	<b>Gd</b>	( $\mu\text{g g}^{-1}$ )	16	<b>Br</b>	( $\mu\text{g g}^{-1}$ )	4
<b>Al<sub>2</sub>O<sub>3</sub></b>	(wt.%)	15.90	<b>Zr</b>	( $\mu\text{g g}^{-1}$ )	1188	<b>Nd</b>	( $\mu\text{g g}^{-1}$ )	92	<b>Yb</b>	( $\mu\text{g g}^{-1}$ )	15	<b>Tb</b>	( $\mu\text{g g}^{-1}$ )	3
<b>CaO</b>	(wt.%)	12.99	<b>V</b>	( $\mu\text{g g}^{-1}$ )	1081	<b>Zn</b>	( $\mu\text{g g}^{-1}$ )	58	<b>U</b>	( $\mu\text{g g}^{-1}$ )	15	<b>Rb</b>	( $\mu\text{g g}^{-1}$ )	3
<b>SiO<sub>2</sub></b>	(wt.%)	6.12	<b>Ni</b>	( $\mu\text{g g}^{-1}$ )	902	<b>Cu</b>	( $\mu\text{g g}^{-1}$ )	54	<b>Sm</b>	( $\mu\text{g g}^{-1}$ )	15	<b>Lu</b>	( $\mu\text{g g}^{-1}$ )	2
<b>TiO<sub>2</sub></b>	(wt.%)	5.78	<b>Ce</b>	( $\mu\text{g g}^{-1}$ )	439	<b>Co</b>	( $\mu\text{g g}^{-1}$ )	40	<b>Te</b>	( $\mu\text{g g}^{-1}$ )	13	<b>Tm</b>	( $\mu\text{g g}^{-1}$ )	2
<b>Na<sub>2</sub>O</b>	(wt.%)	2.86	<b>Ba</b>	( $\mu\text{g g}^{-1}$ )	234	<b>Ga</b>	( $\mu\text{g g}^{-1}$ )	39	<b>Er</b>	( $\mu\text{g g}^{-1}$ )	13	<b>Se</b>	( $\mu\text{g g}^{-1}$ )	2
<b>Total C</b>	(wt.%)	1.53	<b>As</b>	( $\mu\text{g g}^{-1}$ )	164	<b>Hf</b>	( $\mu\text{g g}^{-1}$ )	30	<b>Cs</b>	( $\mu\text{g g}^{-1}$ )	13	<b>Cd</b>	( $\mu\text{g g}^{-1}$ )	0.5
<b>LOI</b>	(wt.%)	13.6	<b>Sr</b>	( $\mu\text{g g}^{-1}$ )	131	<b>W</b>	( $\mu\text{g g}^{-1}$ )	30	<b>Ta</b>	( $\mu\text{g g}^{-1}$ )	8	<b>Ag</b>	( $\mu\text{g g}^{-1}$ )	0.3
<b>MgO</b>	(wt.%)	0.21	<b>Pb</b>	( $\mu\text{g g}^{-1}$ )	120	<b>Sb</b>	( $\mu\text{g g}^{-1}$ )	26	<b>Ge</b>	( $\mu\text{g g}^{-1}$ )	8	<b>Hg</b>	(ng g <sup>-1</sup> )	40
<b>P<sub>2</sub>O<sub>5</sub></b>	(wt.%)	0.12	<b>La</b>	( $\mu\text{g g}^{-1}$ )	115	<b>Pr</b>	( $\mu\text{g g}^{-1}$ )	24	<b>Bi</b>	( $\mu\text{g g}^{-1}$ )	7	<b>Au</b>	(ng g <sup>-1</sup> )	bdl
<b>K<sub>2</sub>O</b>	(wt.%)	0.08	<b>Sc</b>	( $\mu\text{g g}^{-1}$ )	114	<b>Dy</b>	( $\mu\text{g g}^{-1}$ )	20	<b>Be</b>	( $\mu\text{g g}^{-1}$ )	5	<b>ΣLREE*<sup>1</sup></b>	( $\mu\text{g g}^{-1}$ )	<b>704</b>
<b>Total S</b>	(wt.%)	0.07	<b>Th</b>	( $\mu\text{g g}^{-1}$ )	111	<b>Sn</b>	( $\mu\text{g g}^{-1}$ )	19	<b>Ho</b>	( $\mu\text{g g}^{-1}$ )	4	<b>ΣHREE*<sup>2</sup></b>	( $\mu\text{g g}^{-1}$ )	<b>157</b>
<b>MnO</b>	(wt.%)	0.03	<b>Nb</b>	( $\mu\text{g g}^{-1}$ )	106	<b>Mo</b>	( $\mu\text{g g}^{-1}$ )	17	<b>Eu</b>	( $\mu\text{g g}^{-1}$ )	4	<b>ΣREE*<sup>3</sup></b>	( $\mu\text{g g}^{-1}$ )	<b>976</b>

\*<sup>1</sup> ΣLREE group includes the lanthanide elements from La through Gd<sup>8,9</sup>.

\*<sup>2</sup> ΣHREE group includes the lanthanide elements from Tb through Lu, including Y<sup>8,9</sup>.

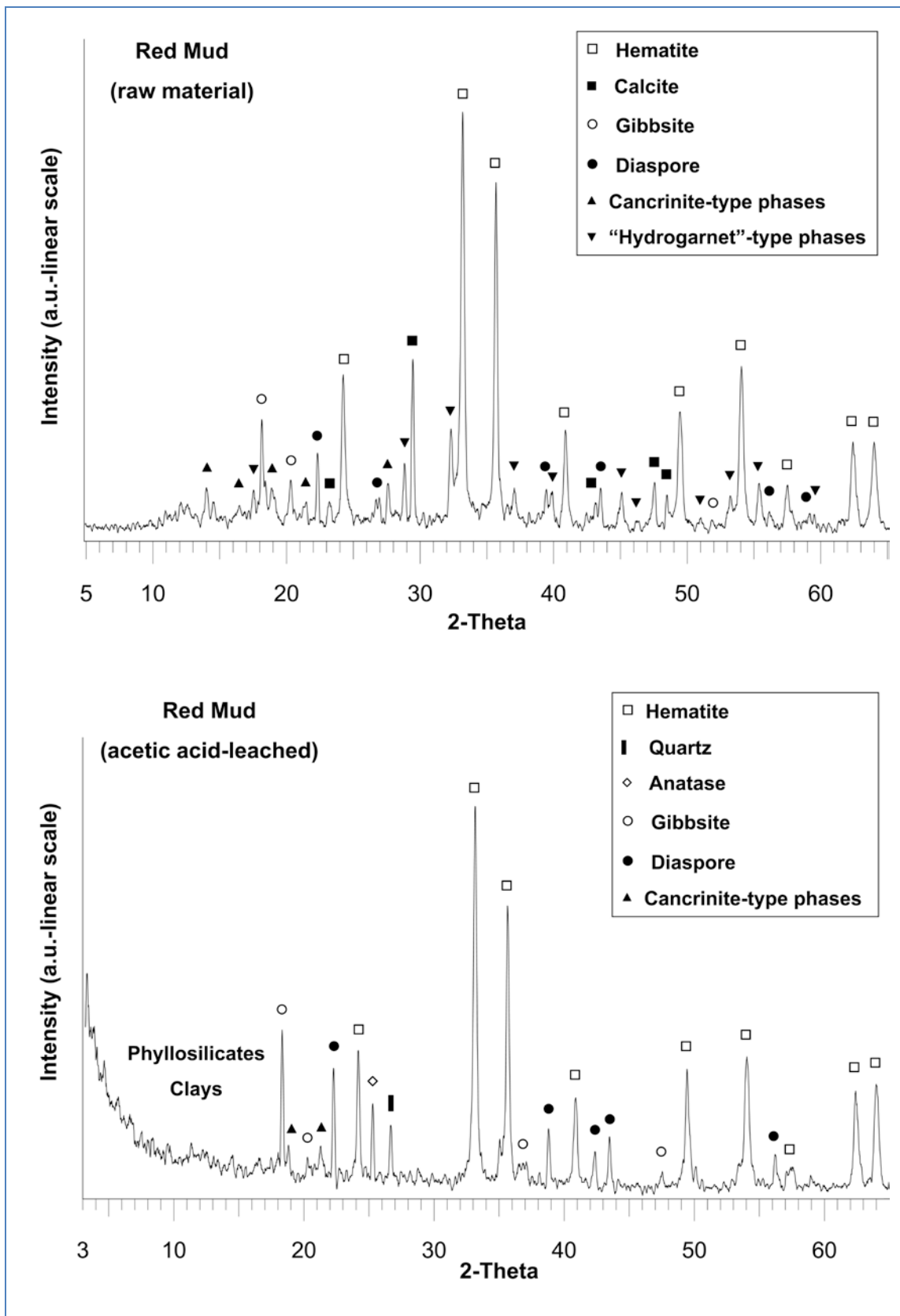
\*<sup>3</sup> ΣREE group comprises of the 15 lanthanide elements including Sc, and Y<sup>8,9</sup>.

**Supplementary Table S4:** Natural radionuclides (Bq kg<sup>-1</sup>) and total dose rate (nGy h<sup>-1</sup>) of the studied bauxite residue / BR (red mud) and representative Greek bauxites ( $n=10$ )<sup>10</sup> compared with relevant values from literature<sup>2,11-25</sup>.

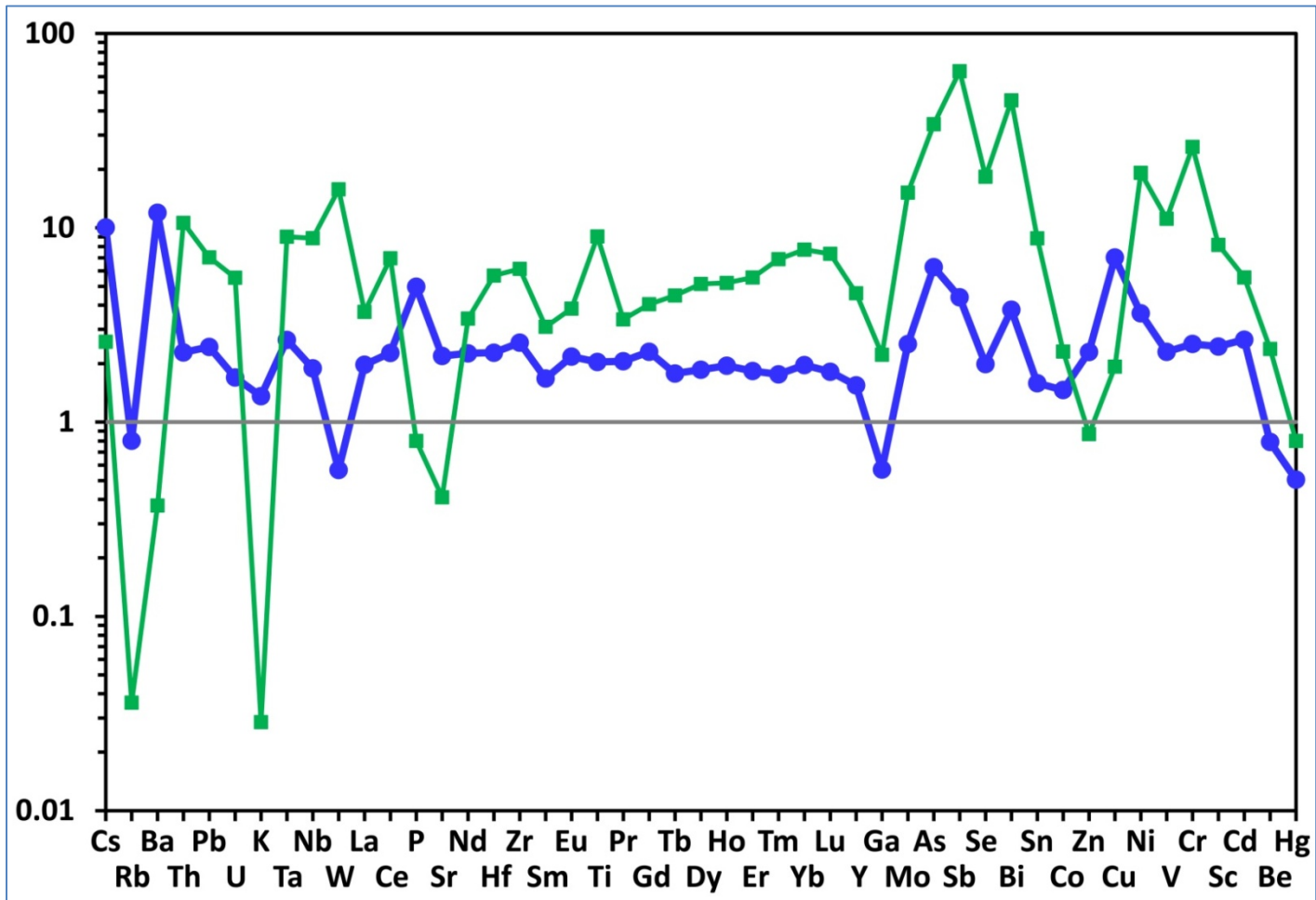
<b>GREEK BAUXITES: Radioactivity (Bq kg<sup>-1</sup>) &amp; Total Dose Rate (nGy h<sup>-1</sup>)</b>							
<b><u>Greek bauxites (present study)</u></b>		<b><sup>232</sup>Th</b>	<b><sup>238</sup>U</b>	<b><sup>226</sup>Ra</b>	<b><sup>40</sup>K</b>	<b><sup>137</sup>Cs</b>	<b>Total Dose</b>
<b>Sample Code</b>	<b>Sample Description</b>	<b>(due to <sup>228</sup>Ac)</b>	<b>(due to <sup>234</sup>Th)</b>				<b>Rate</b>
ALM0306_PL1_B1	<i>Low grade; Fe-rich; Diasporic; Red-brown</i>	192	69	138	15	0	174
ALM0306_PL1_B3	<i>Low grade; Fe-rich; Diasporic; Red-brown</i>	184	89	130	57	0	177
ELM0206_DV_B1	<i>Low grade; Fe-rich; Diasporic; Red-brown</i>	179	44	115	15	0	154
SAB0306_ASV	<i>Low grade; Fe-rich; Diasporic; Red-brown</i>	203	42	96	16	0	162
ALM0306_PL1_B2	<i>Low grade; Fe-rich; Boehmitic; Red-brown</i>	159	54	129	60	0	151
ELM0206_KV_B1	<i>Low grade; Fe-rich; Boehmitic; Red-brown</i>	155	27	64	109	0	130
ELM0206_2H1	<i>Low grade; Fe-rich; Boehmitic; Red-brown</i>	161	60	145	108	0	150
SAB0306_SKR	<i>Low grade; Fe-rich; Boehmitic; Red-brown</i>	166	38	83	49	0	137
ALM0306_PL1_BIW	<i>High grade; Fe-depleted; Diasporic; White-grey</i>	229	121	144	17	0	200
ALM0306_PL1_BS2	<i>High grade; Fe-depleted; Diasporic; White-grey</i>	191	118	160	12	0	186
<b>Min – Max Values</b>		<b>155 – 229</b>	<b>27 – 121</b>	<b>64 – 160</b>	<b>17 – 117</b>	<b>0</b>	<b>130 – 200</b>
<b>Average Value</b>		<b>182</b>	<b>66</b>	<b>120</b>	<b>46</b>	<b>0</b>	<b>162</b>
<b><u>Greek bauxites (previous works)</u></b>							
Greek bauxites <sup>11</sup>		205 – 226	143 – 248	74 – 150	28		

Supplementary Table S4: (continued)

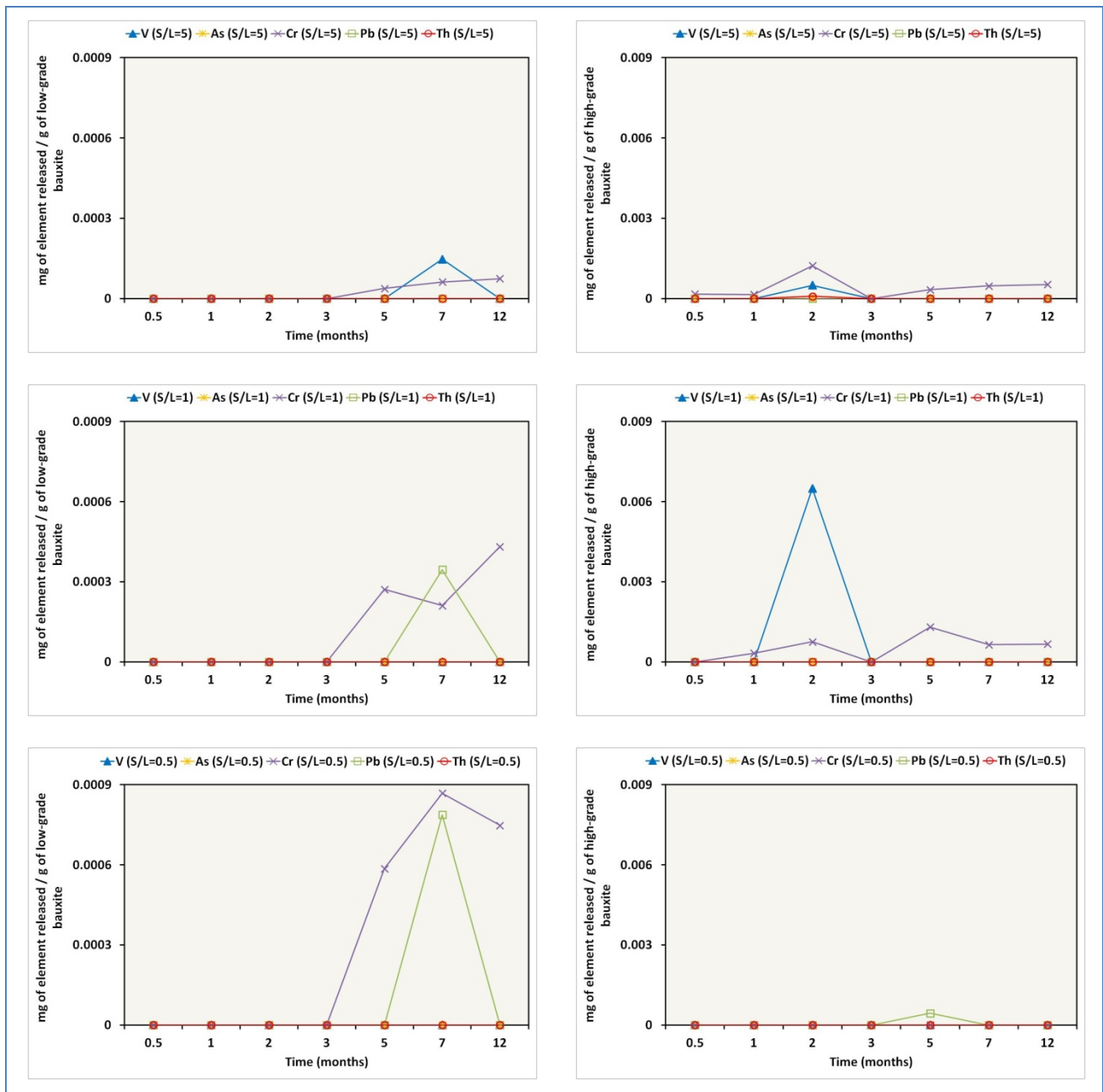
<b>Bauxite Residue / BR (Red Mud)</b>						
<b>Radioactivity (Bq kg<sup>-1</sup>) &amp; Total Dose Rate (nGy h<sup>-1</sup>)</b>						
<b><u>Greece</u></b>						
<b>Red Mud - Greece (present study)</b>	<b>355</b>	<b>133</b>	<b>171</b>	<b>45</b>	<b>0</b>	<b>295</b>
Red Mud - Greece <sup>11</sup>	15 – 412	52 – 400	13 – 185	72 – 160	1 – 5	
Red Mud - Greece <sup>2</sup>	472	149	379	21		
Red Mud - Greece <sup>12</sup>	346	182	232	45		
<b><u>Worldwide</u></b>						
Red Mud - Turkey <sup>13</sup>	539	218	210	112		
Red Mud - Turkey <sup>14</sup>	342 – 357		128 – 285	94 – 110		
Red Mud - Hungary <sup>15</sup>	219 – 392		225 – 568	5 – 101		
Red Mud - Hungary <sup>16</sup>	285 – 380		150 – 700	5 – 101		
Red Mud - Hungary <sup>16</sup>	87 – 545		102 – 506	47 – 212		
Red Mud - Hungary <sup>17</sup>	640	550		250	5.5	
Red Mud - Spain <sup>18</sup>	598	350	203	62		
Red Mud - Germany <sup>19</sup>	183	85	122			
Red Mud - Jamaica <sup>20</sup>	328 – 350		370 – 1047	265 – 335		
Red Mud - Australia <sup>21</sup>	1129		326	30		
Red Mud - Australia <sup>22</sup>		400	310	350		
Red Mud - Australia <sup>23</sup> and refs therein	1000 – 1900	150 – 600		70 – 230		
Red Mud - China <sup>24</sup>	705	477		153		
Red Mud - China <sup>25</sup>	360 – 475		125 – 620	67 – 247		



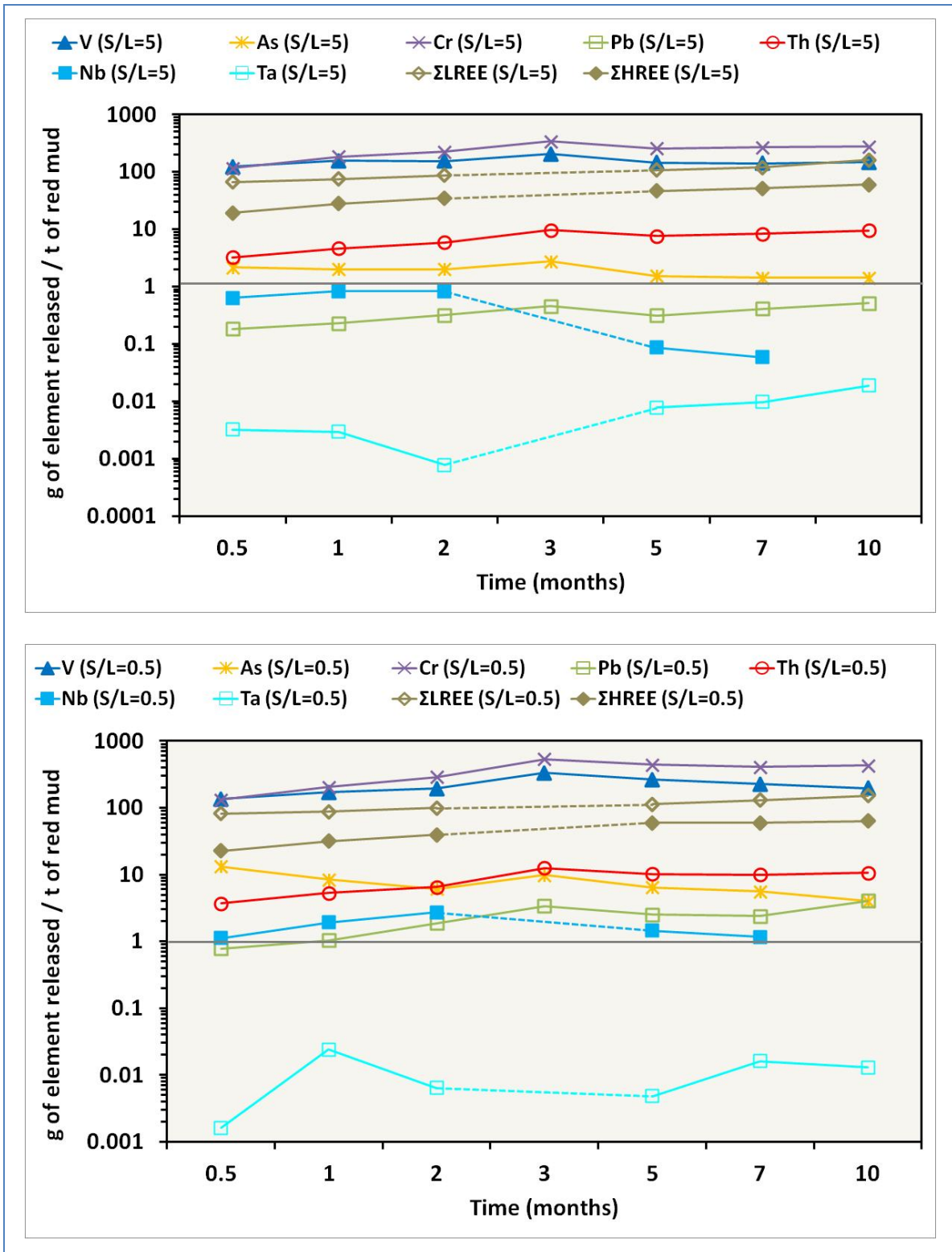
**Supplementary Figure 1** | PXRD pattern of the studied bauxite residue / BR (red mud) from Greece (raw material: upper image) and the acetic acid-leached sample (lower image).



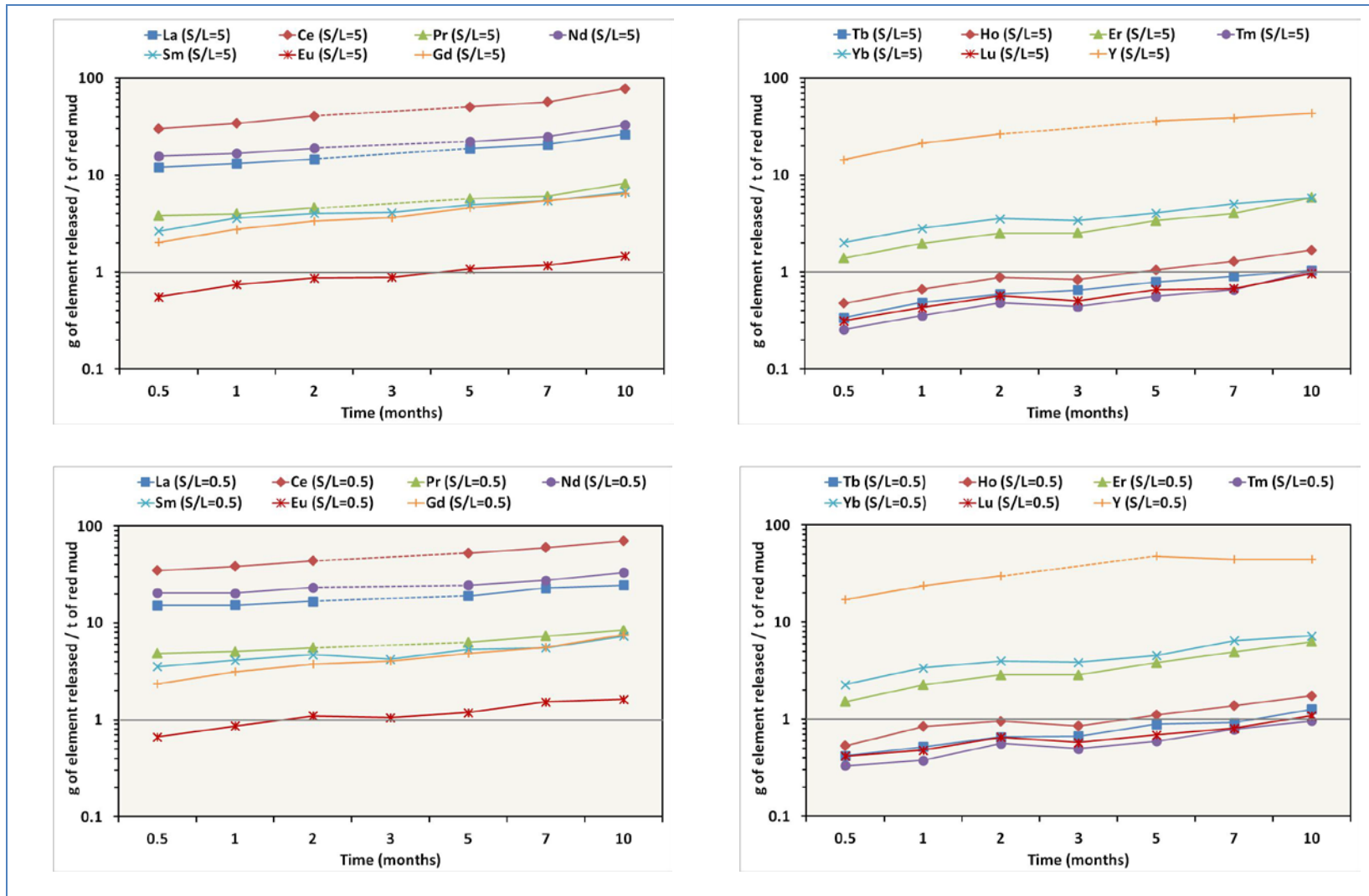
**Supplementary Figure 2** | Spider diagrams of the studied bauxite residue / BR elemental content normalized: (a) to the average ( $n=16$ )<sup>10</sup> of the chemical composition of Greek bauxites from the Parnassos-Ghiona area, solid blue circles; (b) to the reference values of Upper Continental Crust/UCC<sup>26</sup>, solid green squares.



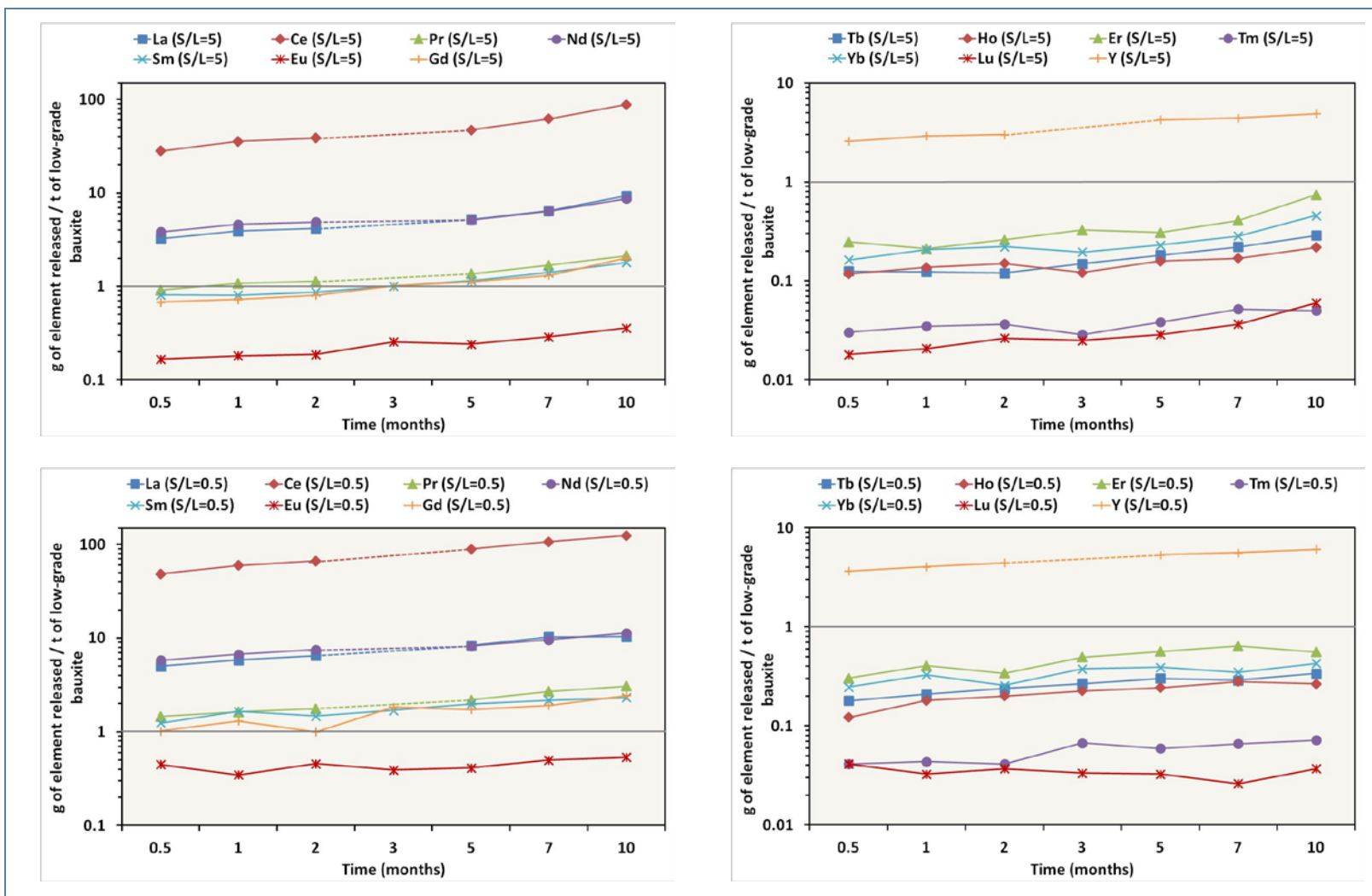
**Supplementary Figure 3** | Results from leaching experiments showing the V, As, Cr, Pb, and Th negligible release from typical low-grade (left images) and high-grade (right images) Greek bauxite leached by Mediterranean seawater from Greece.



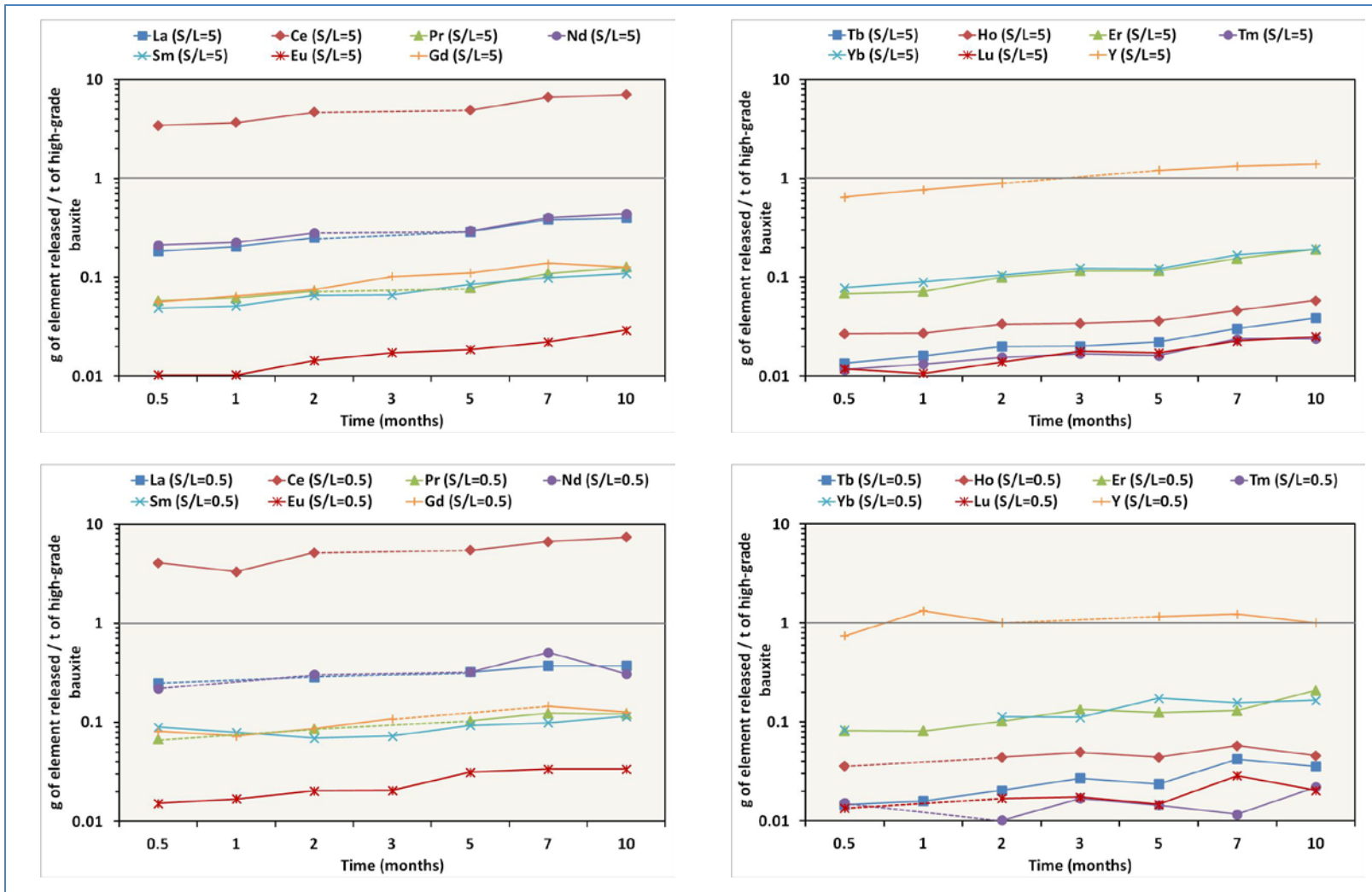
**Supplementary Figure 4** | Results from leaching experiments showing the release of ΣLREE, and ΣHREE, along with with Cr, V, Th, As, Pb, Nb, and Ta from Greek bauxite residue / BR (red mud) leached by concentrated acetic acid.



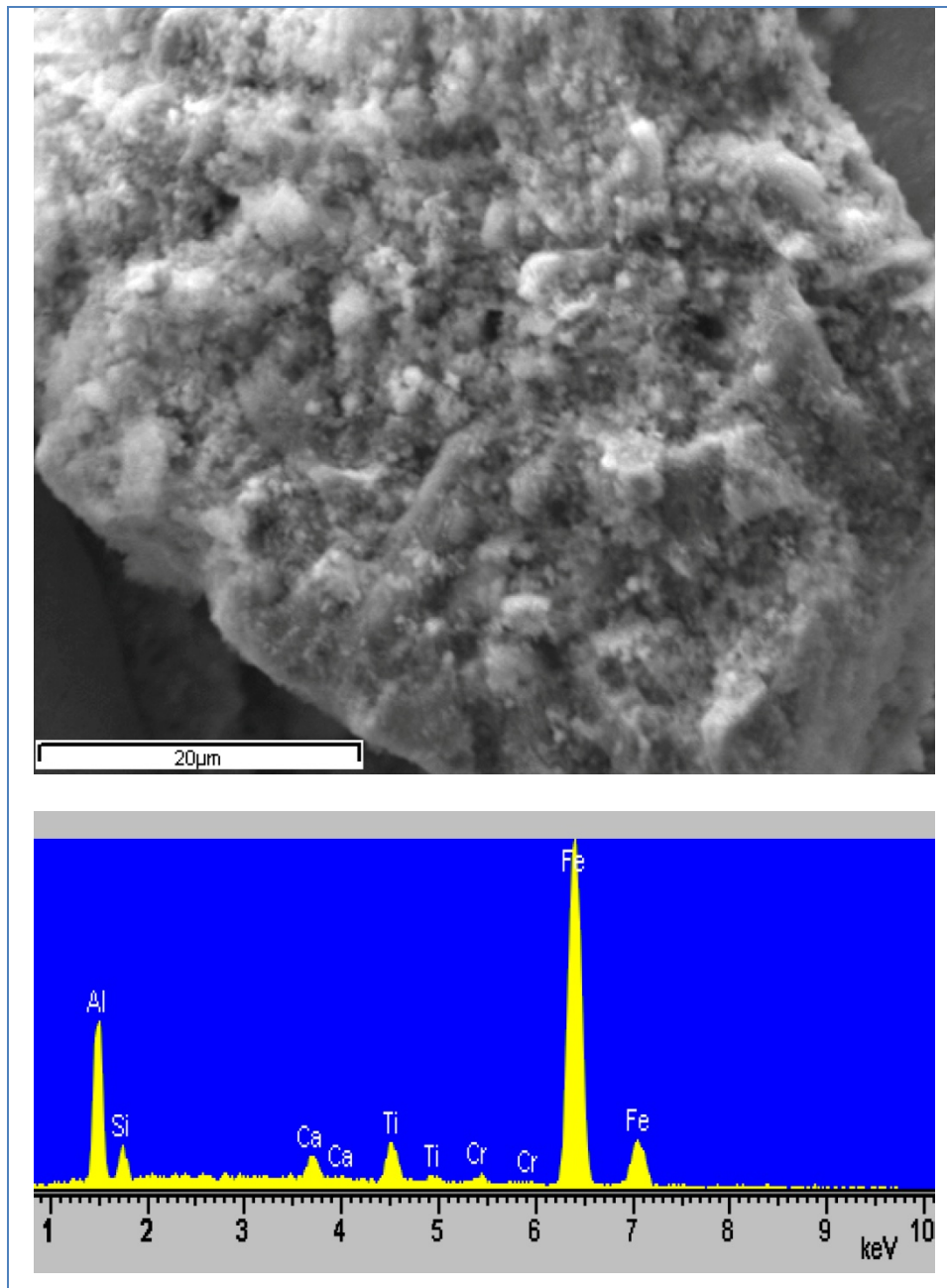
**Supplementary Figure 5** | Results from leaching experiments showing the LREE (La, Ce, Pr, Nd, Sm, Eu, and Gd; left images) as well as the HREE (Tm, Yb, Lu, and Y; right images) release (g) per 1 ton of Greek bauxite residue / BR (red mud) leached by concentrated acetic acid.



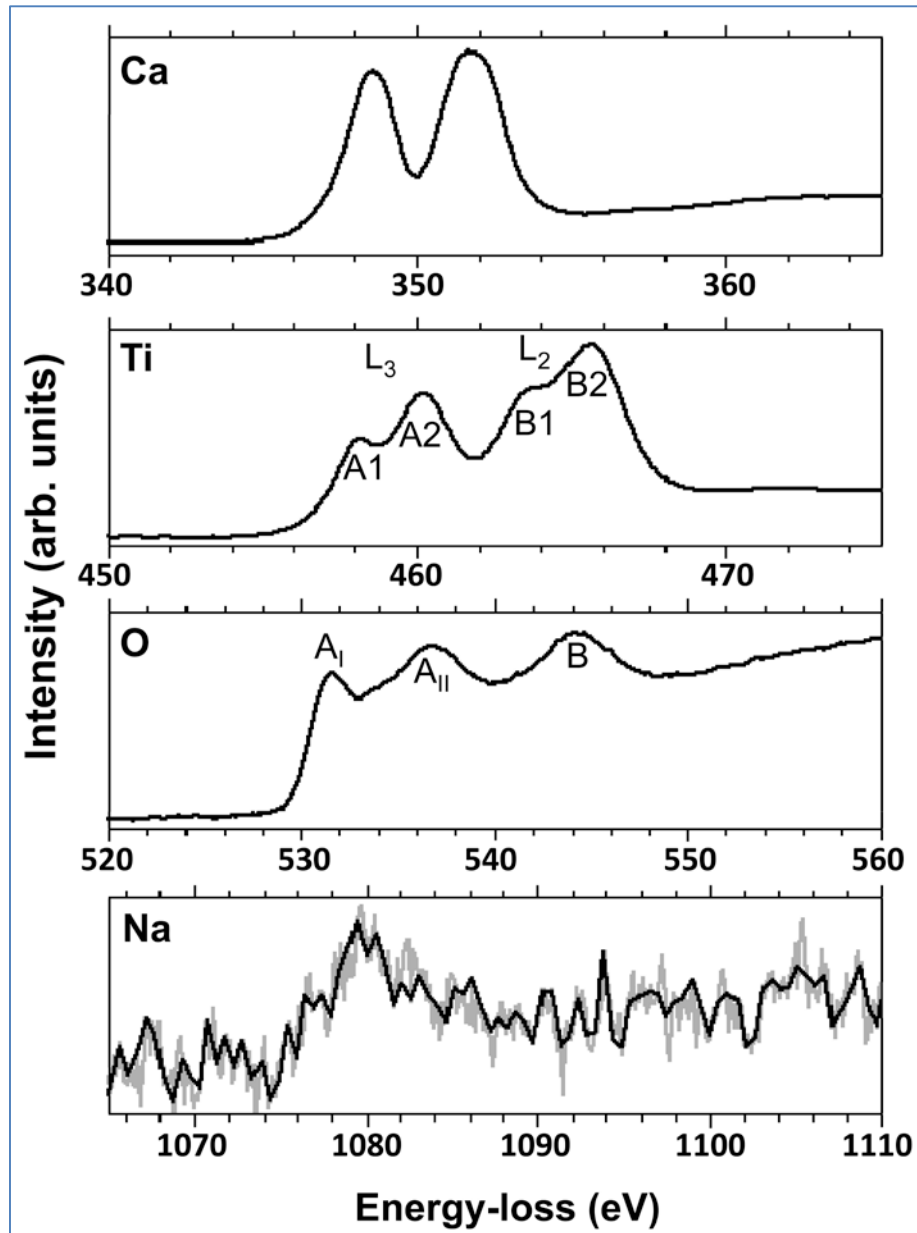
**Supplementary Figure 6** | Results from leaching experiments, relative to S/L ratio effect, showing the LREE (La, Ce, Pr, Nd, Sm, Eu, and Gd; left images) as well as the HREE (Tr, Ho, Er, Tm, Yb, Lu, and Y; right images) release from Greek typical low-grade bauxites leached by concentrated acetic acid.



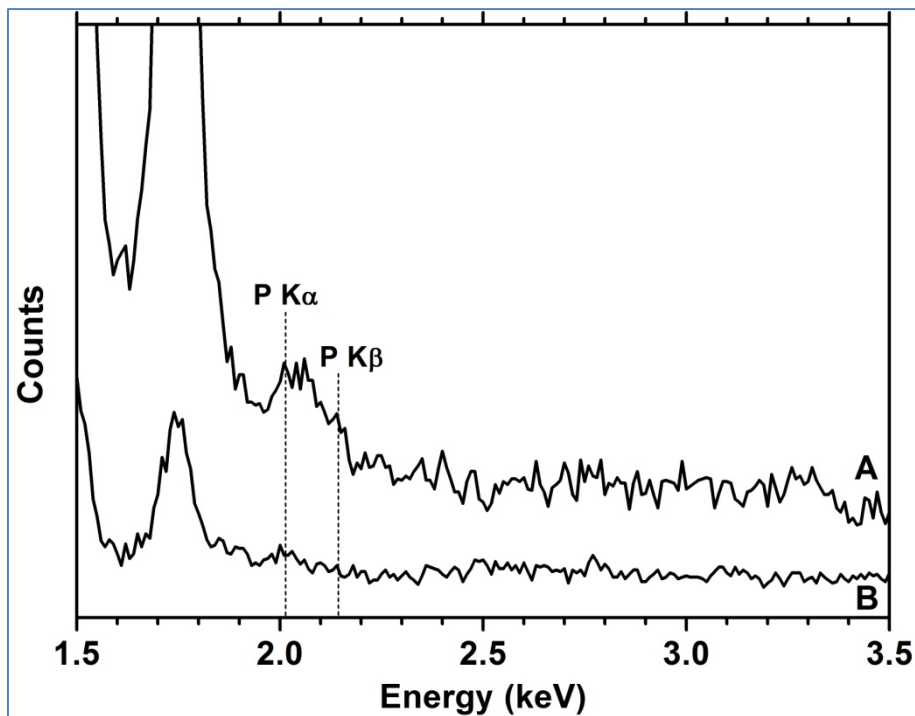
**Supplementary Figure 7** | Results from leaching experiments, relative to S/L ratio effect, showing the LREE (La, Ce, Pr, Nd, Sm, Eu, and Gd; left images) as well as the HREE (Tr, Ho, Er, Tm, Yb, Lu, and Y; right images) release from Greek high-grade bauxites leached by concentrated acetic acid.



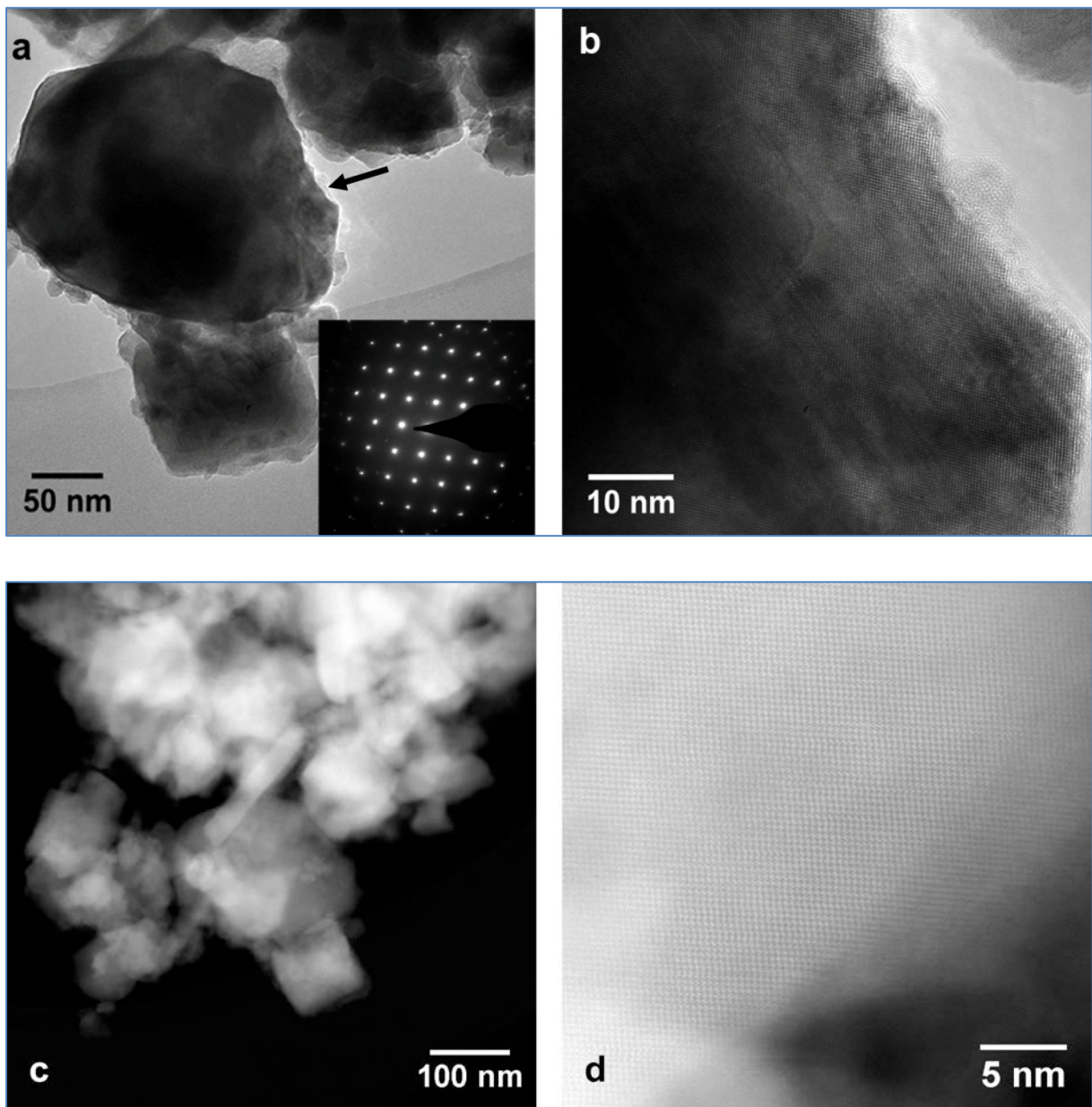
**Supplementary Figure 8** | Morphology and chemical composition (major elements) of the studied bauxite residue / BR (red mud) by SEM-EDS at the microscale, after acid-leaching.



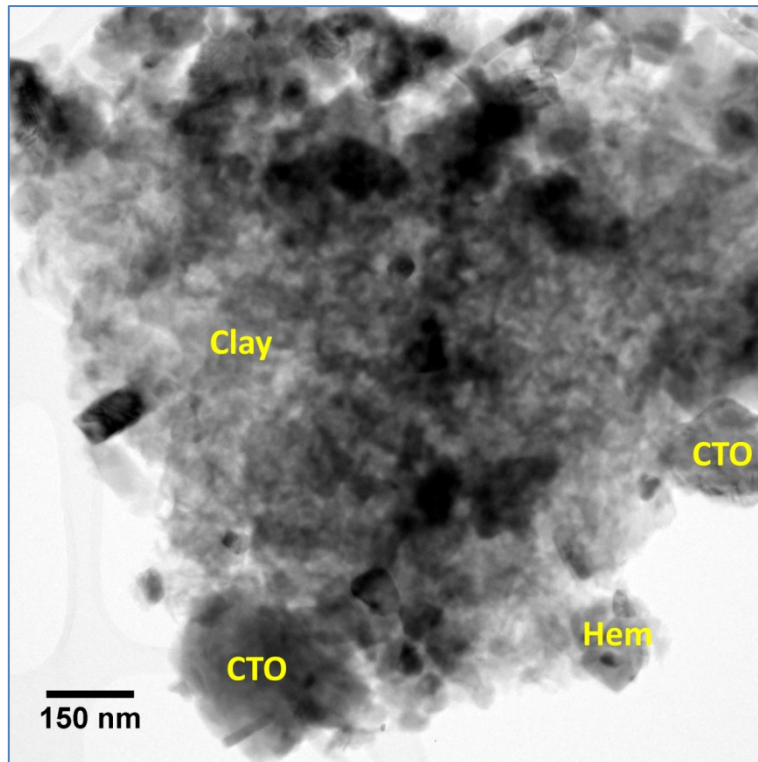
**Supplementary Figure 9** | Representative Ca  $L_{2,3}$ -, Ti  $L_{2,3}$ -, O  $K$ - and Na  $K$ -edge EEL spectral data of the nano-perovskite in the Greek bauxite residue / BR (red mud).



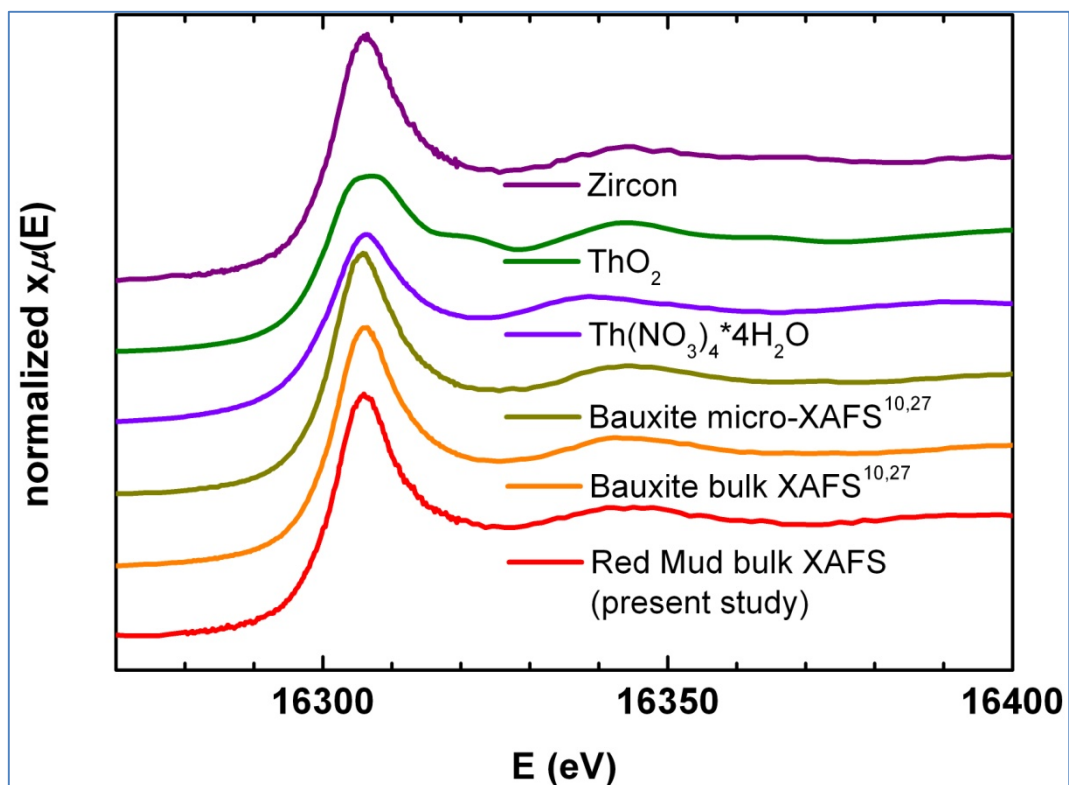
**Supplementary Figure 10** | The appearance of the P K $\alpha$  peak (2.01 KeV) at the STEM-EDS spectrum of a Ti-containing hematite particle (**A**: hematite [211]; see also **Fig. 4**), in contrast to the absence of the P K $\alpha$  peak at the STEM-EDS spectrum of another Ti-containing hematite particle (**B**: hematite [241]). Both the Ti-containing hematite particles observed in the “Al-Fe-Ca-Ti-Si-Na-Cr matrix” of the studied Greek bauxite residue / BR (red mud). A small contribution from the P K $\beta$  peak (2.14 KeV) at the Ti-containing hematite [211] cannot be excluded.



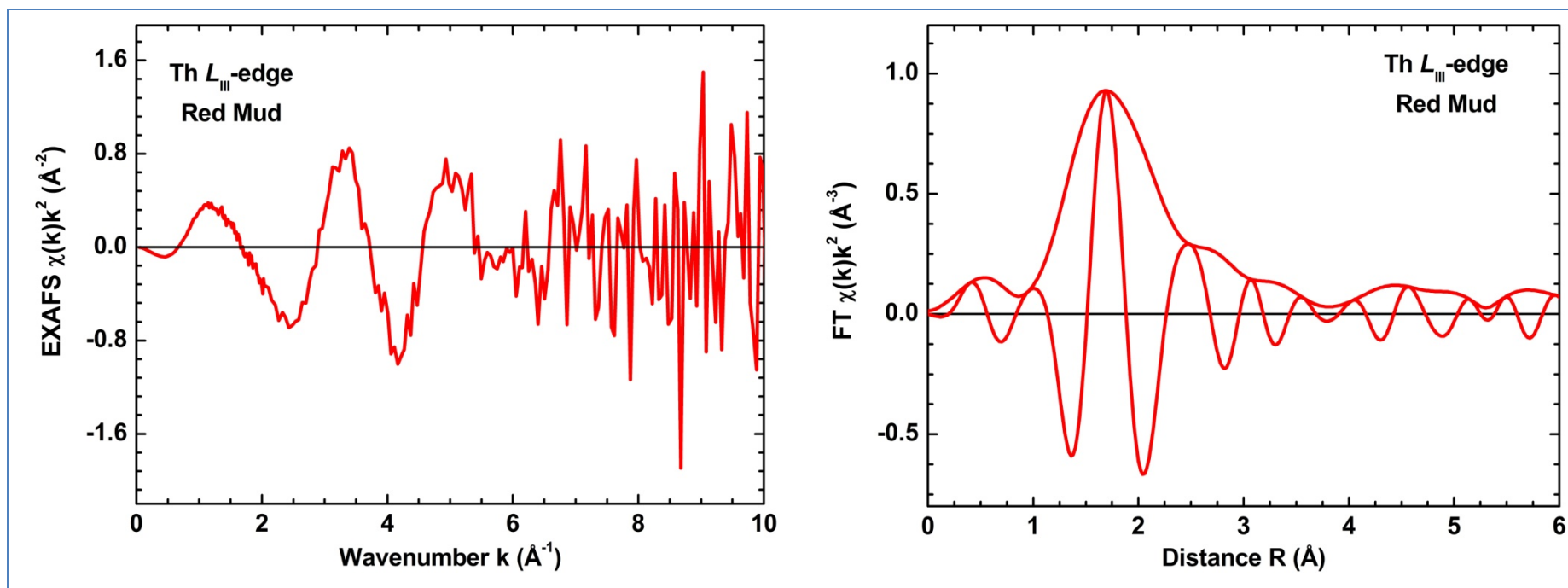
**Supplementary Figure 11** | *Upper images*: HRTEM data, including a BF image and its SAED pattern (a), of a representative Ti-oxide particle (anatase /  $\text{TiO}_2$ ), which exists in the “Al-Fe-Ca-Ti-Si-Na-Cr matrix” of the studied Greek bauxite residue / BR (red mud). The viewing direction for its SAED pattern is [111]. Several planar defects, common in anatase, can be observed in the HRTEM image (b). *Lower images*: STEM-HAADF images of the anatase, showing no apparent sign of Th. The HAADF contrast is proportional to the square of a mean atomic number.



**Supplementary Figure 12** | BF image of the Th-free clay-like phases together with nano-perovskite (CTO) and Th-free Ti-containing hematite (Hem) co-existing into the “Al-Fe-Ca-Ti-Si-Na-Cr matrix” of the studied Greek bauxite residue / BR (red mud).



**Supplementary Figure 13** | Th  $L_{III}$ -edge bulk XANES of the studied Greek bauxite residue / BR (red mud; present study) together with bulk & micro-XANES of Greek bauxite<sup>10,27</sup>, compared with spectra of reference materials.



**Supplementary Figure 14** | Experimental Th  $L_{III}$ -edge EXAFS spectrum (left image) and its Fourier transform – FT (right image) of the studied bauxite residue / BR (red mud).

## Supplementary References

1. Grew, E. S. *et al.* Nomenclature of the garnet supergroup. *Am. Mineral.* **98**, 785-811 (2013).
2. Pontikes, Y., Vangelatos, I., Boufounos, D., Fafoutis, D. & Angelopoulos, G. N. Environmental aspects on the use of Bayer's process bauxite residue in the production of ceramics. Paper presented at: The 11<sup>th</sup> International Ceramics Congress, Sicily, Italy. Switzerland: Trans Tech Publications. (DOI:10.4028/www.scientific.net/AST.45.2176) (2006, June 4-9)
3. Burke, I. T. *et al.* Speciation of arsenic, chromium, and vanadium in red mud samples from the Ajka spill site, Hungary. *Environ. Sci. Technol.* **46**, 3085-3092 (2012).
4. Liang, W. *et al.* Effect of strong acids on red mud structural and fluoride adsorption properties. *J. Colloid Interf. Sci.* **423**, 158-165 (2014).
5. Smičiklas, I. *et al.* Effect of acid treatment on red mud properties with implications on Ni(II) sorption and stability. *Chem. Engineer. J.* **242**, 27-35 (2014).
6. Calvert, C. C., Rainforth, W. M., Sinclair, D. C. & West, A. R. EELS characterization of bulk  $\text{CaCu}_3\text{Ti}_4\text{O}_{12}$  ceramics. *Micron.* **37**, 412-419 (2006).
7. Mariano, A. N. & Mariano, A. Jr. Rare earth mining and exploration in North America. *Elements.* **8**, 369-376 (2012).
8. Gambogi, J. 2012 *Minerals Yearbook: Rare Earths [Advance Release]*. U.S. Department of the Interior, USGS, Technical Report. (2015) Available at: [http://minerals.usgs.gov/minerals/pubs/commodity/rare\\_earth/myb1-2012-raree.pdf](http://minerals.usgs.gov/minerals/pubs/commodity/rare_earth/myb1-2012-raree.pdf). (Accessed: 24<sup>th</sup> February 2015)
9. Zepf, V. (2013) Rare Earth Elements: What and where they are. In *Rare Earth Elements: A new approach to the nexus of supply, demand, and use: Exemplified along the use of Neodymium in permanent magnets*; Zepf, V., Ed.; Springer Theses; Springer-Verlag Berlin Heidelberg, 2013; pp 11-39.
10. Gamaletsos, P. Mineralogy and geochemistry of bauxites from Parnassos-Ghiona mines and the impact on the origin of the deposits. Ph.D. Thesis, University of Athens, Greece, 2014.
11. Papatheodorou, G., Papaefthymiou, H., Maratou, A. & Ferentinos, G. Natural radionuclides in bauxitic tailings (red-mud) in the Gulf of Corinth, Greece. *Radioprotection.* **40**, 549-555 (2005).

12. Samouhos, M., Taxiarchou, M., Tsakiridis, P. E. & Potiriadis, K. Greek "red mud" residue: A study of microwave reductive roasting followed by magnetic separation for a metallic iron recovery process. *J. Hazard. Mater.* **254-255**, 193-205 (2013).
13. Akinci, A. & Artir, R. Characterization of trace elements and radionuclides and their risk assessment in red mud. *Mater. Charact.* **59**, 417-421 (2008).
14. Turhan, Ş., Arkan, İ. H., Demirel, H. & Güngör, N. Radiometric analysis of raw materials and end products in the Turkish ceramics industry. *Radiat. Phys. Chem.* **80**, 620-625 (2011).
15. Somlai, J., Jobbágy, V., Kovács, J., Tarján, J. & Kovács, T. Radiological aspects of the usability of red mud as building material additive. *J. Hazard. Mater.* **150**, 541-545 (2008).
16. Jobbágy, V., Somlai, J., Kovács, J., Szeiler, G. & Kovács, T. Dependence of radon emanation of red mud bauxite processing wastes on heat treatment. *J. Hazard. Mater.* **172**, 1258-1263 (2009).
17. Ruyters, S. *et al.* The red mud accident in Ajka (Hungary): plant toxicity and trace metal bioavailability in red mud contaminated soil. *Environ. Sci. Technol.* **45**, 1616-1622 (2011).
18. Rubinos, D. A. & Barral, M. T. Fractionation and mobility of metals in bauxite red mud. *Environ. Sci. Pollut. Res.* **20**, 7787-7802 (2013).
19. Von Philipsborn, H. & Kühnast, E. Gamma spectrometric characterization of industrially used African and Australian bauxites and their red mud tailings. *Radiat. Prot. Dosim.* **45**, 741-743 (1992).
20. Pinnock, W. R. Measurements of radioactivity in Jamaican building materials and gamma dose equivalents in a prototype red mud house. *Health Phys.* **61**, 647-651 (1991).
21. Beretka, J. & Mathew, P. J. Natural radioactivity of Australian building materials, industrial wastes and by-products. *Health Phys.* **48**, 87-95 (1985).
22. Cooper, M. B., Clarke, P. C., Robertson, W., McPharlin, I. R. & Jeffrey, R. C. An investigation of radionuclide uptake into food crops grown in soils treated with bauxite mining residues. *J. Radioanal. Nucl. Chem.* **194**, 379-387 (1995).
23. Cooper, M. B. *Naturally Occurring Radioactive Materials (NORM) in Australian Industries - Review of Current Inventories and Future Generation*, Radiation Health and Safety Advisory Council,

Technical Report. (2005) Available at: [http://www.arpansa.gov.au/pubs/norm/cooper\\_norm.pdf](http://www.arpansa.gov.au/pubs/norm/cooper_norm.pdf).  
(Accessed: 21<sup>st</sup> December 2005)

24. Wang, K. Levels of radioactivity in the red mud and red mud cement and its dose rate for local residents. *Huanjing Kexue*. **13**, 90-93 (1992).

25. Wang, P. & Liu, D. -Y. Physical and chemical properties of sintering red mud and Bayer red mud and the implications for beneficial utilization. *Materials*. **5**, 1800-1810 (2012).

26. Rudnick, R. & Gao, S. Composition of the continental crust in *Treatise on Geochemistry*, Vol. 3 (eds Holland, H. D. & Turekian, K. K.) 1-64 (Elsevier, 2003).

27. Gamaletsos, P. *et al.* Thorium partitioning in Greek industrial bauxite investigated by synchrotron radiation and laser-ablation techniques. *Nucl. Instrum. Meth. B*. **269**, 3067-3073 (2011).